

PanSplat: 4K Panorama Synthesis with Feed-Forward Gaussian Splatting

Cheng Zhang^{1,2} Haofei Xu³ Qianyi Wu^{1*}

Camilo Cruz Gambardella^{1,2} Dinh Phung¹ Jianfei Cai¹

¹Monash University ²Building 4.0 CRC, Caulfield East, Victoria, Australia ³ETH Zurich



Figure 1. **Our PanSplat can generate novel views from two 4K (2048 × 4096) panoramas.** We train on rendered Matterport3D [10] data at 4K resolution (left) and can generalize to 4K real-world data (right) with a few fine-tunings on 360Loc [27] data (Zoom in for details). Please refer to the supplementary video for more results.

Abstract

With the advent of portable 360° cameras, panorama has gained significant attention in applications like virtual reality (VR), virtual tours, robotics, and autonomous driving. As a result, wide-baseline panorama view synthesis has emerged as a vital task, where high resolution, fast inference, and memory efficiency are essential. Nevertheless, existing methods are typically constrained to lower resolutions (512 × 1024) due to demanding memory and computational requirements. In this paper, we present **PanSplat**, a generalizable, feed-forward approach that efficiently supports **resolution up to 4K** (2048 × 4096). Our approach features a tailored spherical 3D Gaussian pyramid with a Fibonacci lattice arrangement, enhancing image quality while reducing information redundancy. To accommodate the demands of high resolution, we propose a pipeline that integrates a hierarchical spherical cost volume and Gaussian heads with local operations, enabling two-step de-

ferred backpropagation for memory-efficient training on a single A100 GPU. Experiments demonstrate that PanSplat achieves state-of-the-art results with superior efficiency and image quality across both synthetic and real-world datasets. Code will be available at <https://github.com/chengzhag/PanSplat>.

1. Introduction

The demand for rich visual content for virtual reality (VR) and virtual tours has surged alongside the rise of 360° cameras and immersive technologies. Panoramic light field systems [9, 44] offer compelling solutions for delivering realistic, immersive experiences, by enabling users to explore environments from a range of arbitrary viewpoints within designated virtual spaces. Recent advancements in 360° cameras simplify immersive content creation, driving applications like street view (Google Maps [3], Apple Maps [1]) and virtual tours (Matterport [4], Theasys [5]), where novel view synthesis from wide-baseline panoramas is essential

*Corresponding author.

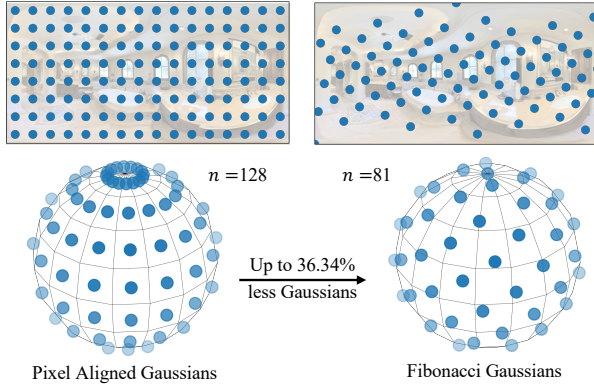


Figure 2. **Fibonacci Gaussians.** We propose a Fibonacci lattice arrangement for the Gaussians to be distributed uniformly across the sphere, avoiding information redundancy near the poles, and significantly reducing the number of required Gaussians.

for providing smooth transitions between locations.

While current methods have extensively explored wide-baseline panorama view synthesis, they often struggle to balance computational efficiency, memory consumption, image quality, and resolution. Conventional methods [7, 23, 34, 36] rely on explicit 3D scene representations such as Multi-Plane Images (MPI) [7, 23, 36] or mesh [34], which offer potential scalability to high resolutions but often yield lower image quality due to limited expressiveness. Neural Radiance Fields (NeRF)-based methods [16], by contrast, deliver high-quality results but are computationally demanding and memory-intensive, making them less suitable for high-resolution panoramas. Most existing methods are limited to a maximum resolution of 512×1024 , which is well below 4K (2048×4096), a resolution typically needed in VR applications for a truly immersive experience.

Recent trends in 3D Gaussian Splatting (3DGS) [31] have shown promising results in synthesizing novel views, marking a significant advancement in image quality and computational efficiency. By representing scenes as collections of Gaussian primitives, 3DGS uses rasterization instead of volumetric sampling of NeRF to achieve high-quality, highly efficient rendering while also enabling differentiable rendering for training. Subsequent works have further pushed the boundaries of 3DGS by introducing feed-forward networks [11, 15, 35, 51, 56, 61, 64, 70] to predict Gaussians directly from input images, extending it to sparse view inputs. Despite these advancements, existing 3DGS methods are not directly applicable to panoramas due to two primary challenges: 1) the unique spherical geometry of panoramas, which conflicts with pixel-aligned Gaussians and results in overlapping and redundant Gaussians near the poles; 2) the high-resolution demand of VR applications, which makes it infeasible for current methods (*e.g.*, MVSplat [15]) to scale efficiently due to memory limitations.

In this work, we present **PanSplat**, a feed-forward approach optimized for 4K resolution inputs, generating a 3D Gaussian representation specifically tailored for panoramic formats to enable 4K novel view synthesis from wide-baseline panoramas (see examples in Fig. 1). To address the first challenge, we introduce a Fibonacci lattice arrangement for 3D Gaussians (illustrated in Fig. 2), significantly reducing the required Gaussians by uniformly distributing them across the sphere. On the other hand, to enhance rendering quality, we implement 3D Gaussian pyramid, which represents the scene at multiple scales, capturing fine details across varying levels. To address the second challenge, we utilize a hierarchical spherical cost volume built on a transformer-based network to estimate high-resolution 3D geometry with improved efficiency. We then design Gaussian heads with local operations to predict Gaussian parameters, enabling two-step deferred backpropagation for memory-efficient training at 4K resolution. Additionally, we introduce a deferred blending technique that reduces artifacts from misaligned Gaussians due to moving objects and depth inconsistencies, enhancing rendering quality in real-world scenes.

Our main contributions can be summarized as follows.

- We present PanSplat, a feed-forward approach that efficiently generates high-quality novel views with spherical 3D Gaussian pyramid tailored for panorama formats.
- We design a pipeline featuring a hierarchical spherical cost volume and Gaussian heads with local operations, which enables a two-step deferred backpropagation, efficiently scaling to higher resolutions.
- We demonstrate that PanSplat achieves state-of-the-art results with superior image quality across synthetic and real-world datasets, with up to $70\times$ faster inference speed compared to the SOTA method [16]. By supporting 4K resolution, PanSplat becomes a promising solution for immersive VR applications.

2. Related Work

Sparse Perspective Novel View Synthesis. The task of novel view synthesis has been widely explored for perspective images. Recent methods such as NeRF [41] and 3DGS [31] have achieved remarkable results but rely heavily on dense input views, making them costly for real-world applications. To address this limitation, many approaches [11, 12, 14, 15, 20, 35, 39, 42, 51, 52, 55–57, 60, 64, 66, 70] have emerged that leverage prior knowledge from large-scale datasets to handle sparse input views. These include per-scene optimization methods [20, 42, 52, 57, 66] that optimize a scene-specific model, as well as feed-forward methods [11, 12, 14, 15, 35, 39, 51, 55, 56, 60, 64, 70] that directly predict novel views from sparse inputs. While these methods simplify data capture requirements, optimization-based approaches remain computationally ex-

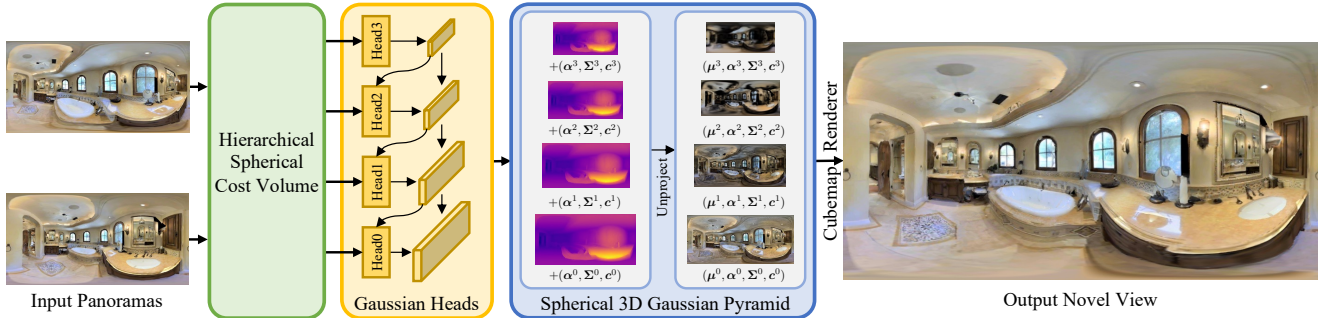


Figure 3. **Our proposed PanSplat pipeline.** Given two wide-baseline panoramas, we first construct a hierarchical spherical cost volume (Sec. 3.2) using a Transformer-based FPN to extract feature pyramid and 2D U-Nets to integrate monocular depth priors for cost volume refinement. We then build Gaussian heads (Sec. 3.3) to generate a feature pyramid, which is later sampled with Fibonacci lattice and transformed to spherical 3D Gaussian pyramid (Sec. 3.1). Finally, we unproject the Gaussian parameters for each level and view, consolidate them into a global representation, and splat it into novel views using a cubemap renderer. *For simplicity, intermediate results of only a single view are shown.*

pensive and require significant time to train a model specific to each scene. Feed-forward methods like NeuRay [39], IBRNet [55], and MV3Splat [15], on the other hand, are more efficient by utilizing pre-trained models that generalize well across different scenes. Despite recent advancements, these methods are not directly applicable to panoramas due to their distinct spherical geometry. Our approach builds upon the feed-forward 3DGS framework, extending it to high-resolution panoramas by introducing a tailored spherical 3D Gaussian pyramid and a hierarchical spherical cost volume. While concurrent work [51] also explores hierarchical 3D Gaussians as a more expressive representation, it does not address the unique challenges of high-resolution or panoramic formats.

Sparse Panorama Novel View Synthesis. Recently, the panorama format has gained significant attention as it becomes more accessible and valuable in applications like VR, virtual tours, and autonomous driving, with numerous works focusing on generation [24, 50, 65, 68], out-painting [6, 19, 43, 53, 54, 58], and reconstruction [21, 29, 32, 62, 67]. However, novel view synthesis for panoramas has received less attention compared to perspective images, largely due to the challenges in efficiently processing high-resolution equirectangular images. Existing methods [8, 13, 17, 18, 26, 37] have focused on per-scene optimization, addressing the distinct spherical geometry of panoramas. Further advancements have been made for sparse panorama inputs, such as SOMSI [23], which takes a set of panorama images and represents 3D scene with a Multi-Sphere Images (MSI) representation. OmniSyn [34] further reduces the input requirement to two wide-baseline panoramas, but the less expressive mesh representation limits the quality of novel views. Following this setting, PanoGRF [16] enhances image quality with a spherical NeRF and combines a monocular and stereo depth model to improve geometry, but is computationally expensive due to volumetric sampling of NeRF. Although existing methods

have paved the way for real-world applications with wide-baseline panorama inputs, they are still limited to low resolutions and do not generalize well to real-world datasets. In contrast, our PanSplat is designed to efficiently handle high-resolution panoramas, capable of providing a realistic and immersive experience.

3. Method

PanSplat is a feed-forward model that synthesizes high-quality novel views efficiently from two posed wide-baseline panoramas as shown in Fig. 3. We introduce a spherical 3D Gaussian pyramid (Sec. 3.1) specifically tailored for panoramic images, which we pair with a hierarchical spherical cost volume (Sec. 3.2) and Gaussian heads (Sec. 3.3) to enable scalable, high-resolution output up to 4K for real-world applications. The training procedure is described in detail in Sec. 3.4.

3.1. Spherical 3D Gaussian Pyramid

Fibonacci Gaussians. Recall that current pixel-aligned Gaussian splatting methods [11, 15, 70] assign a Gaussian to each pixel (top-left of Fig. 2), where each Gaussian is defined by parameters including center μ , opacity α , covariance Σ , and color c . Such representation is inefficient for panoramas, as pixel density varies with latitude, leading to redundant Gaussians near the poles, as shown in the bottom-left of Fig. 2. Instead, we propose to distribute the Gaussians using a Fibonacci lattice [2, 45] to achieve a more uniform distribution across the sphere (bottom-right of Fig. 2), which significantly reduces Gaussian redundancy, particularly near the poles (top-right of Fig. 2). Specifically, we set the number of Gaussian $n = \lfloor W^2/\pi \rfloor$ based on image resolution, where W is the panorama image width, to ensure Gaussian density near the equator is similar to that of image pixels. The value of n can be adjusted to balance image quality and rendering efficiency. Then, for the j -th

Gaussian on the Fibonacci lattice, its coordinates on the image plane are calculated as $(x_j, y_j) = \left(\frac{j}{\phi} \bmod 1, \frac{j}{n-1}\right)$, where $\phi = \frac{1+\sqrt{5}}{2}$ is the golden ratio. This configuration reduces Gaussian usage by up to 36.34% compared to pixel-aligned splatting without compromising image quality (see +Fibo in Tab. 3).

3D Gaussian Pyramid. To further enhance image quality, we draw inspiration from [28] to introduce a pyramid structure that captures multi-scale details. Given two input panoramas $\{\mathbf{I}_i\}_{i=0}^1 \in \mathbb{R}^{H \times W \times 3}$, we aim to predict Gaussian parameters $\{(\boldsymbol{\mu}_i^l, \boldsymbol{\alpha}_i^l, \boldsymbol{\Sigma}_i^l, \mathbf{c}_i^l)\}_{l=0, i=0}^{L-1, 1}$ at different levels l for each view i . To estimate the Gaussian centers $\boldsymbol{\mu}$, we first predict a depth for each Gaussian and then unproject the image-plane coordinates (x_j, y_j) into 3D space. We define the number of Gaussians at level l as $n^l = \lfloor W^2 / (2^l \pi) \rfloor$, with the number of pyramid levels set to $L = 4$. Each level is designed to represent a specific level of details, ranging from the coarsest level, $l = 3$, with the fewest Gaussians, to the finest level, $l = 0$, which has the highest Gaussian density.

3.2. Hierarchical Spherical Cost Volume

To support the proposed pyramid representation and meet the high-resolution demands of real-world applications, we construct a hierarchical spherical cost volume that efficiently estimates 3D geometry at a higher resolution than MVSpLat [15].

Feature Pyramid Extraction. We first apply a Feature Pyramid Network (FPN) [38] to extract multi-scale features from the input panoramas $\{\mathbf{I}_i\}_{i=0}^1$. At the coarsest level of the FPN, we introduce a Swin Transformer [40] with cross-view attention, enabling effective information exchange between the two panoramas for improved matching. We denote the image feature pyramid as $\{\mathbf{F}_i^l\}_{l=0}^{L-1} \in \mathbb{R}^{H/2^l \times W/2^l \times C^l}$, where C^l represents the number of channels at level l . The feature pyramid is designed to match the L levels of the Gaussian pyramid, serving as an additional input for predicting Gaussian parameters in Sec. 3.3.

Spherical Cost Volume Initialization. Building on this feature representation, we proceed to construct a hierarchical cost volume [22, 63], beginning at the coarsest level $l = 3$. For each reference view $i = 0, 1$, we uniformly sample D inverse depth candidates within a preset range $[d_{\min}, d_{\max}]$ and warp the coarsest feature maps \mathbf{F}_{1-i}^3 to the corresponding reference view using spherical projection [16, 34]. We then calculate the correlations to reference features \mathbf{F}_i^3 via a dot product [59], resulting in a cost volume $\mathbf{C}_i^3 \in \mathbb{R}^{H/8 \times W/8 \times D}$ for each view. To regularize the cost volume in occluded or texture-less regions, we integrate pre-trained monocular depth features [30]. Specifically, a 2D U-Net [46] takes in the concatenated monocular depth features, cost volume, and reference features, and

produces a residual that refines the cost volume. The refined cost volume $\tilde{\mathbf{C}}_i^3$ is then normalized with `softmax` along the depth dimension, yielding the probability distribution of object surfaces across different depths, which we use to weight and average the depth candidates, resulting in the initial depth prediction \mathbf{D}_i^3 .

Hierarchical Cost Volume Refinement. We refine the depth predictions at progressively finer levels $l = 2, 1$, where each level searches near the coarse depth from the previous level and generates a higher-resolution cost volume. Specifically, we up-sample \mathbf{D}_i^{l+1} to the next level l , then construct a more compact cost volume with $D/2^{3-l}$ depth candidates within a reduced range $(d_{\max} - d_{\min})/2^{3-l}$. Independent 2D U-Net for each level is then used to refine the cost volume, with an additional input \mathbf{D}_i^{l+1} to provide contextual information. This process ultimately yields a cost volume $\tilde{\mathbf{C}}_i^1 \in \mathbb{R}^{H/2 \times W/2 \times D/4}$ for each view, along with depth predictions $\{\mathbf{D}_i^l\}_{l=1}^3$ across different levels. To balance memory consumption with depth accuracy, we skip refinement at the finest level $l = 0$, achieving $2\times$ depth resolution compared to MVSpLat under a similar memory budget.

3.3. Gaussian Parameter Prediction and Rendering

Gaussian Heads. After constructing the hierarchical cost volume, we design light-weight Gaussian heads to predict Gaussian parameters at different levels for each view. At level l , we resize the cost volume $\tilde{\mathbf{C}}_i^l$ and the input image \mathbf{I}_i to match the resolution of the image feature \mathbf{F}_i^l , then concatenate them as input. Since we define Gaussians on a Fibonacci lattice, we do not predict the Gaussian parameters in a pixel-aligned manner. Instead, for each level, we use a CNN to first extract a feature map $\tilde{\mathbf{F}}_i^l$, then interpolate a feature vector for each Gaussian, followed by a fully connected layer to predict the Gaussian parameters. So far, we assume that the different layers of Gaussians can represent different levels of details in the scene to improve the rendering quality. However, we find that the network does not fully utilize the multi-scale information (Sec. E in supplementary material), which is likely due to the lack of guidance between different levels. Therefore, we introduce a residual design by up-sampling the feature map $\tilde{\mathbf{F}}_i^{l+1}$ from the previous level, concatenating it as an additional input to the current level Gaussian head, and predicting a residual based on this feature map. This design functions as a skip connection, enforcing dependencies between adjacent levels and guiding the network to leverage the multi-scale structure in a coarse-to-fine manner.

Cubemap Renderer. We consolidate the Gaussian parameters from two input views and different levels of Gaussian heads to form a single Gaussian representation, which we then render in novel views using a cubemap renderer. Specifically, we first render 6 cameras with 90° field of

view (FOV) at the same position but facing different directions defined by the cubemap faces. Then we stitch the cubemap into a panorama with differentiable grid sampling operation (see Sec. B in the supplementary material for details). Although existing methods [8, 37] provide renderers with improved splatting accuracy for panoramas, they are not designed for memory efficiency. In contrast, we reduce memory consumption for high-resolution training by integrating the cubemap renderer and the Gaussian heads with a two-step deferred backpropagation approach.

Two-step Deferred Backpropagation. Based on the observation that image quality relies more on texture resolution than on geometry resolution, we leverage the decoupled design of geometry (hierarchical cost volume) and appearance (Gaussian heads) to scale efficiently to higher resolutions. Specifically, we down-sample the input image for the hierarchical cost volume to 512×1024 while preserving the input resolution for the Gaussian heads. Between the two modules, image features and cost volumes from the former are up-sampled to match the resolution of the latter. This approach allows the finest level of Gaussians to be predicted using full-resolution images as input, preserving detailed texture information, while the geometry is estimated at a lower resolution to maintain reasonable memory usage. Although this design significantly reduces memory consumption (see PanSplat in Fig. 6), it still falls short of handling 4K resolution due to the considerable memory demands of both the Gaussian heads and the Gaussian renderer. For inference, we exploit the local operations of Gaussian heads to enable tiled operations, while the cubemap renderer supports sequential face rendering, both contributing to enhanced memory efficiency. Inspired by [35, 69], we further design a two-step deferred backpropagation to enable memory-efficient training at 4K resolution. In this approach, we first disable auto-differentiation to render the full panorama, compute the image loss, and cache gradients on the image. Subsequently, we enable auto-differentiation and backpropagate gradients in a “two-step” manner: first, the panorama is re-rendered face by face, backpropagating and accumulating gradients to the Gaussian parameters; second, the Gaussian parameters are re-generated tile by tile, with gradients backpropagated and accumulated to the network parameters.

Deferred blending. Due to the omnidirectional nature of panoramas, it is inevitable to include moving objects when capturing real datasets, *e.g.*, camera operators, pedestrians, or vehicles. In this scenario, the two input views would produce inconsistent depth and misaligned Gaussians, leading to artifacts in the rendered images. To mitigate this issue, we draw inspiration from [55] and introduce a deferred blending approach. For details, please refer to Sec. F in the supplementary material.

3.4. Training

Synthetic Data. We follow PanoGRF [16] to train PanSplat on synthetic data with depth and image losses. For depth supervision, we use L_1 loss on the depth predictions from three-level hierarchical cost volume:

$$\mathcal{L}_{\text{depth}} = \sum_{i=0,1} \sum_{l=1}^3 \gamma^{l-1} \left\| D_i^l - \hat{D}_i^l \right\|_1, \quad (1)$$

where \hat{D}_i^l denotes down-sampled ground truth depth, and γ is a weight that emphasizes finer levels. For image supervision, we compute L_2 and LPIPS [71] losses between the rendered image I and the ground truth image \hat{I} :

$$\mathcal{L}_{\text{rgb}} = \left\| I - \hat{I} \right\|_2 + \lambda \text{LPIPS}(I, \hat{I}), \quad (2)$$

We jointly train the network using loss function $\mathcal{L}_{\text{synthetic}} = \alpha \mathcal{L}_{\text{depth}} + \mathcal{L}_{\text{rgb}}$, with $\gamma = 0.9$, $\lambda = 0.1$ and $\alpha = 0.05$.

Real Data. It is challenging to obtain ground truth depth for real-world data. Fortunately, recent works [15, 56] demonstrate that depth estimation can be learned with a self-supervised approach using Gaussian splatting. Since all levels of the hierarchical cost volume require supervision, we propose adding auxiliary Gaussian heads to each level, replacing direct depth loss for training purposes. These auxiliary Gaussian heads operate in parallel with the main Gaussian heads in the network and do not share the same residual design. To enable direct gradient flow, we directly use the predicted depth from the cost volume at each level to unproject Gaussian centers. For simplicity, only 2 CNN layers are used to predict the other Gaussian parameters. The predicted Gaussians from each level are then separately rendered to panoramas $\{I^l\}_{l=1}^3$ and compared with the ground truth using image loss \mathcal{L}_{rgb} . The final loss function becomes

$$\mathcal{L}_{\text{real}} = \sum_{l=1}^3 \gamma^{l-1} \mathcal{L}_{\text{rgb}}(I^l, \hat{I}) + \mathcal{L}_{\text{rgb}}(I, \hat{I}). \quad (3)$$

4. Experiment

4.1. Experimental Setup

Datasets. For comparison with existing methods, we evaluate PanSplat on three synthetic datasets: Matterport3D [10], Replica [47], and Residential [23], all at a resolution of 512×1024 . We follow the data split of PanoGRF [16] to train on Matterport3D with a baseline (distances between input views) of 1.0, and evaluate using fixed baselines of 1.0, 1.5, and 2.0 meters. For Replica and Residential, the baselines are 1.0 and approximately 0.3 meters, respectively. In each case, a middle view is used as the target for both training and evaluation. To scale up to 4K resolution on synthetic data, we render a 4K dataset using Matterport3D. For real-world fine-tuning at 4K resolution, we

Dataset	Matterport3D									Replica			Residential					
	Baseline			1.0m			1.5m			2.0m			1.0m			about 0.3m		
	Method	WS-PSNR \uparrow	SSIM \uparrow	LPIPS \downarrow	WS-PSNR \uparrow	SSIM \uparrow	LPIPS \downarrow	WS-PSNR \uparrow	SSIM \uparrow	LPIPS \downarrow	WS-PSNR \uparrow	SSIM \uparrow	LPIPS \downarrow	WS-PSNR \uparrow	SSIM \uparrow	LPIPS \downarrow		
S-NeRF [41]	15.25	0.579	0.546	14.16	0.563	0.580	13.13	0.523	0.607	16.10	0.723	0.443	22.47	0.741	0.435			
OmniSyn [34]	22.90	0.850	0.244	20.31	0.790	0.317	18.91	0.761	0.354	23.17	0.898	0.189	-	-	-			
IBRNet [55]	25.72	0.855	0.258	21.69	0.751	0.382	20.04	0.706	0.431	22.65	0.854	0.291	22.47	0.735	0.498			
NeuRay [39]	24.92	0.832	0.260	21.92	0.766	0.347	19.85	0.715	0.407	25.90	0.899	0.187	22.38	0.753	0.427			
PanoGRF [16]	27.12	0.876	0.195	23.38	0.811	0.282	20.96	0.761	0.352	29.22	0.937	0.134	31.03	0.909	0.207			
MVSplat [15]	29.29	0.912	0.105	22.51	0.807	0.230	13.38	0.595	0.554	31.25	0.958	0.059	31.32	0.906	0.200			
PanSplat	30.01	0.931	0.091	24.76	0.849	0.181	21.19	0.777	0.265	31.67	0.962	0.069	31.36	0.917	0.172			

Table 1. **Quantitative comparisons on synthetic datasets.** All models are trained on Matterport3D with a baseline of 1.0 meter and evaluated on the test set with the same baseline, as well as on wider baselines of 1.5 and 2.0 meters. Additionally, we evaluate on the Replica and Residential datasets to assess generalization to unseen data. Top results are highlighted in **top1**, **top2**, and **top3**.

Dataset	360Loc (avg. 1.40m baseline)				Insta360 (16 frames apart)			
	Method	PSNR \uparrow	WS-PSNR \uparrow	SSIM \uparrow	LPIPS \downarrow	PSNR \uparrow	WS-PSNR \uparrow	SSIM \uparrow
MVSplat [15]	24.13	24.15	0.823	0.170	20.93	20.96	0.786	0.227
PanSplat	24.83	24.85	0.831	0.162	21.62	21.66	0.807	0.217
PanSplat (w/ Deferred BL)	27.35	27.37	0.860	0.127	23.36	23.38	0.822	0.183

Table 2. **Quantitative comparisons on real-world datasets.** We compare with MVSplat, as it does not require depth supervision, which is unavailable for real-world datasets. All models are fine-tuned on the 360Loc dataset and directly tested on the Insta360 dataset for generalization evaluation.

utilize the 360Loc [27] dataset and a self-captured Insta360 dataset. 360Loc contains posed panorama sequences across four scenes, with an average baseline of 0.47 meters. We select one scene as test set and fine-tune PanSplat on the other three scenes, using two views spaced two frames apart as input and evaluating across all four views. We record two videos walking through indoor and outdoor scenes at 24 FPS using a 360° camera (Insta360 X4). For camera pose estimation, we use OpenVSLAM [48] without loop closure. From this dataset, we select two views spaced 15 frames apart as input, evaluating all 17 frames.

Implementation Details. We first train the model on Matterport3D at a height of 256, then fine-tune it at 512. For 4K fine-tuning, we progressively increase the height from 1024 to 2048, with deferred backpropagation enabled. For real datasets, we fine-tune on 360Loc, incrementally raising the resolution from 512 to 2048.

Evaluation Metrics. Following PanoGRF [16], we use PSNR, SSIM [25], LPIPS [71], and WS-PSNR [49] to evaluate image quality, but focus more on WS-PSNR as it considers pixel density of equirectangular images.

4.2. Comparison with Previous Works

Baselines. We compare PanSplat with several feed-forward methods, including PanoGRF [16], NeuRay [39], IBRNet [55], and OmniSyn [34], as well as with an optimization-based method, S-NeRF (PanoGRF’s spherical adaption of NeRF [41]), all at a resolution of 512×1024 . Notably, PanoGRF requires 23.8 seconds to generate an im-

age, whereas PanSplat achieves the same result in just 0.34 seconds (0.32 seconds for the feed-forward network inference and 0.02 seconds for 3DGS rendering), making it up to **70** \times faster. PanSplat enables real-time rendering and achieves a speed that is not feasible for NeRF-based approaches. To compare with the latest 3DGS techniques, we adapt MVSplat [15], a feed-forward method designed for perspective images, by replacing its camera model with a spherical camera and following their protocol to train on Matterport3D and fine-tune on 360Loc. We follow the evaluation protocol of PanoGRF and report their original results of PanoGRF, NeuRay, IBRNet, OmniSyn and S-NeRF.

Quantitative Results. Tab. 1 presents a quantitative comparison on Matterport3D, the dataset all methods are trained on. PanSplat consistently outperforms all competing methods, not only on the training baseline of 1.0 meters but also when generalizing to wider baselines of 1.5 and 2.0 meters. Although MVSplat serves as a strong baseline with recent advancements in 3DGS, it falls notably short of PanSplat’s performance, especially at wider baselines. To further evaluate generalization, we test on Replica and Residential datasets, where PanSplat achieves the best performance across most metrics, highlighting its strong generalization capability. For real-world datasets where depth ground truth is unavailable, we compare with MVSplat, a method also supports training without depth supervision. As shown in Tab. 2, PanSplat consistently outperforms MVSplat across all metrics, with deferred blending (w/ Deferred BL) providing an additional performance boost.

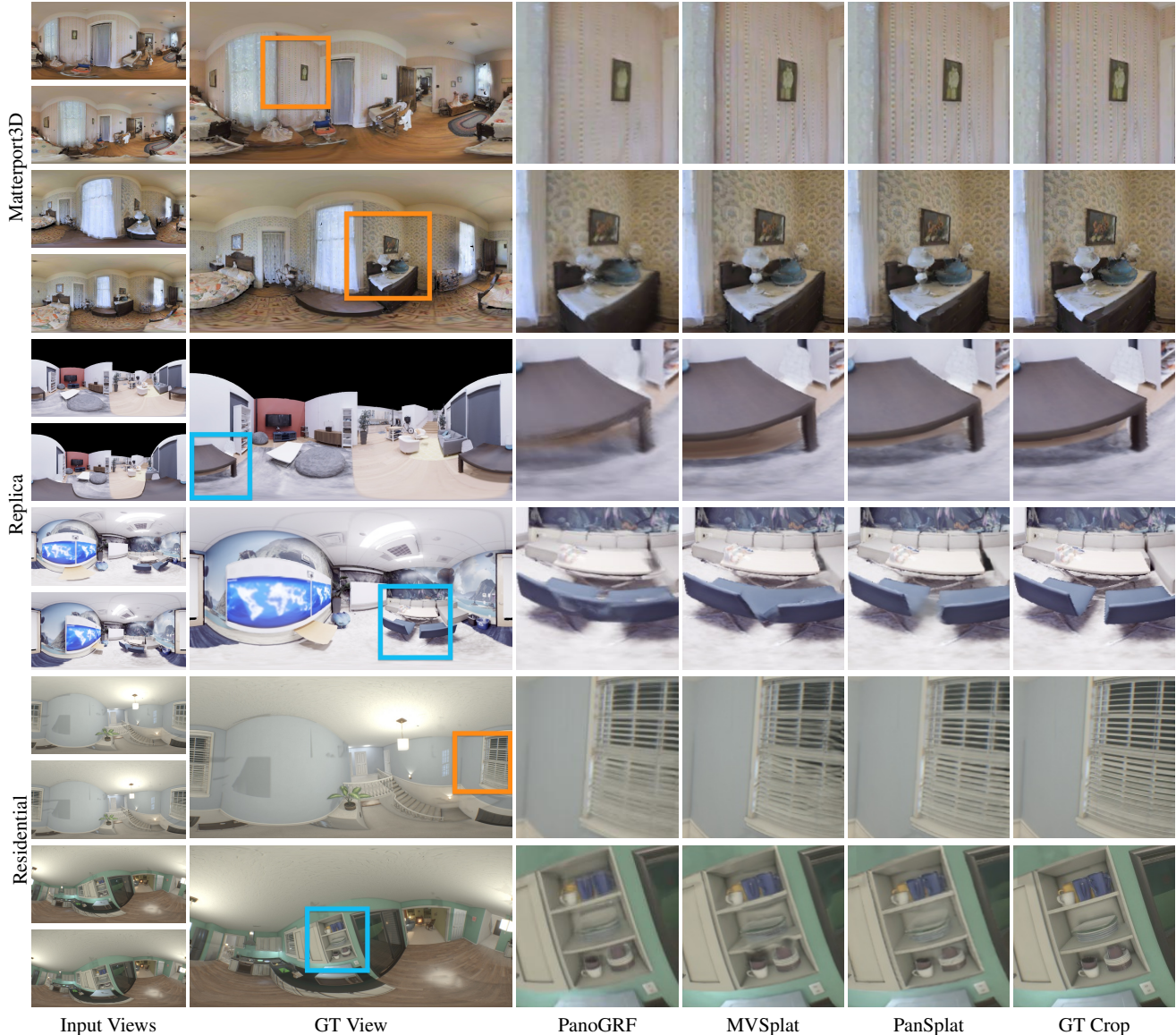


Figure 4. **Qualitative comparisons on synthetic datasets.** We show the input panorama pairs and the ground truth novel views on the left, and compare the zoomed-in results on the right to highlight the differences. Our PanSplat generates overall sharper images with **more high-frequency details** and **improved geometry**.

Qualitative Results. Fig. 4 presents qualitative comparisons on synthetic datasets, where we compare PanSplat with the best-performing baselines, PanoGRF and MVSplat. Overall, Gaussian-based methods (PanSplat and MVSplat) preserve more details and produce sharper images compared to PanoGRF. Furthermore, thanks to the spherical 3D Gaussian pyramid, PanSplat generates **more detailed textures, particularly in high-frequency areas** such as the pattern on the wall in the first and second rows, and the blinds in the fifth row. Besides, the use of a hierarchical spherical cost volume enables **more accurate depth estimation, resulting in improved geometry** in other samples.

4.3. Ablation Study

Synthetic Datasets. We conduct an ablation study on Matterport3D to assess the impact of the two key components: Fibonacci Gaussians and 3D Gaussian pyramid. As shown in Tab. 3, we begin by evaluating a baseline model (Base) without these components, utilizing a single 1/4-resolution cost volume to maintain comparable computational cost and memory usage with the full model. Next, we add Fibonacci Gaussians (+Fibo), which significantly reduces the number of Gaussians without compromising image quality. Finally, we incorporate 3D Gaussian Pyramid (+3DGP) to capture multi-scale details, resulting in further performance im-

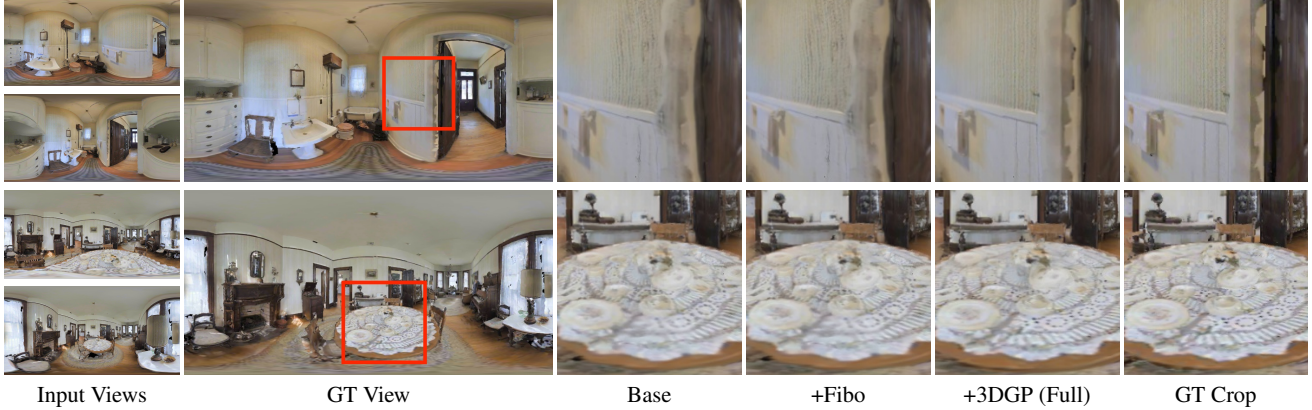


Figure 5. **Qualitative comparisons of ablation study.** Our Fibonacci Gaussians (+Fibo) reduces Gaussian count without compromising image quality, and our 3D Gaussian Pyramid (+3DGP) further enhances quality.

Setup	#Gaussian (K)	WS-PSNR \uparrow	SSIM \uparrow	LPIPS \downarrow
Base	1,049 (100%)	28.20	0.895	0.127
+Fibo	668 (63.67%)	28.99	0.906	0.116
+3DGP (Full)	887 (84.55%)	30.01	0.931	0.091

Table 3. **Ablation study.** We count the number of Gaussians (#Gaussians) and evaluate performance on the Matterport3D 1.0m baseline test set. We progressively add our two proposed components to the base model and measure the performance.

provements. Although 3DGP introduces additional Gaussians, the use of Fibo helps offset the increase, leading to an overall reduction in the total Gaussian count. Fig. 5 presents visual comparisons, where the baseline model fails to capture fine details, whereas the full model with 3DGP generates sharper images with more accurate geometry. It also demonstrates that the use of Fibo does not introduce visible artifacts, highlighting its effectiveness in reducing the number of Gaussians without sacrificing quality.

Real Datasets. In Sec. 4.2 and Tab. 2, we demonstrate that deferred blending (w/ Deferred BL) substantially enhances the performance on real-world datasets. A more detailed analysis of deferred blending’s impact is provided in Sec. F of the supplementary material.

Scaling Up to 4K Resolution. We evaluate the impact of the two-step deferred backpropagation on training memory consumption in Fig. 6. As shown, MVSplat reaches memory overflow at a relatively low resolution of 512×1024 , while PanSplat is able to support 768×1536 resolutions due to its fixed cost volume size and the efficient design of the Gaussian heads. It is worth noting that this design choice does not compromise image quality, as discussed in Sec. 4.2; rather, it enables deferred backpropagation, drastically reducing memory consumption during training and allowing PanSplat to support 4K resolution on a single A100 GPU. We present qualitative 4K results of PanSplat in Fig. 1 and include additional results in the supplementary video.

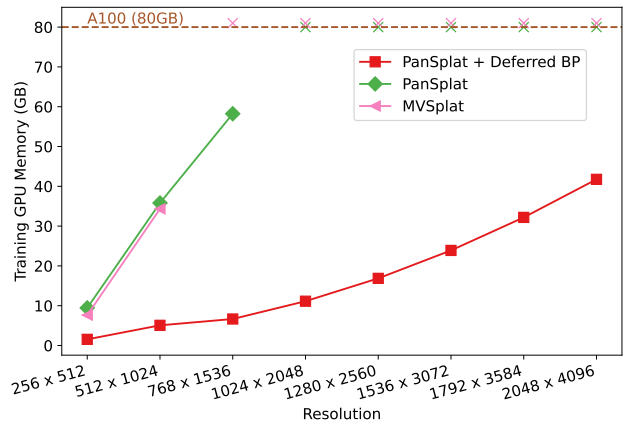


Figure 6. **Training GPU memory consumption at different resolutions,** where \times indicates out-of-memory errors even on a 80GB A100. Memory consumption is tested with a batch size of 1.

We also provide an in-depth analysis of design choices and inference memory usage in Sec. G of the supplementary material, which shows that PanSplat can inference at 4K resolution on a 24GB RTX 3090 GPU.

5. Conclusion

In this paper, we have presented PanSplat, a novel generalizable, feed-forward approach for novel view synthesis from wide-baseline panoramas. To efficiently support 4K resolution (2048×4096) for immersive VR applications, we have introduced a pipeline that enables two-step deferred backpropagation. In addition, we have proposed a spherical 3D Gaussian pyramid with a Fibonacci lattice arrangement tailored for panorama formats, to enhance both rendering quality and efficiency. Extensive experiments have demonstrated the superiority of PanSplat over existing techniques in terms of image quality and resolution.

Limitations. While PanSplat provides a promising solution for high-resolution panoramic novel view synthesis, it lacks

support for dynamic scenes with moving objects, a frequent requirement in real-world applications. Future work could explore extending PanSplat to handle dynamic scenes by incorporating motion-aware representations.

References

- [1] Maps - apple. <https://www.apple.com/maps/>. 1
- [2] Fibonacci Lattices / Amit Sch. <https://observablehq.com/@meetamit/fibonacci-lattices>. 3
- [3] Explore Street View and add your own 360 images to Google Maps. <https://www.google.com/streetview/>. 1
- [4] Capture, share, and collaborate the built world in immersive 3D. <https://matterport.com>. 1
- [5] Theasys - 360 VR Online Virtual Tour Creator. <https://www.theasys.io/>. 1
- [6] Naofumi Akimoto, Yuhi Matsuo, and Yoshimitsu Aoki. Diverse plausible 360-degree image outpainting for efficient 3dgc background creation. In *CVPR*, pages 11441–11450, 2022. 3
- [7] Benjamin Attal, Selena Ling, Aaron Gokaslan, Christian Richardt, and James Tompkin. Matryodshka: Real-time 6dof video view synthesis using multi-sphere images. In *ECCV*, pages 441–459. Springer, 2020. 2
- [8] Jiayang Bai, Letian Huang, Jie Guo, Wen Gong, Yuanqi Li, and Yanwen Guo. 360-gs: Layout-guided panoramic gaussian splatting for indoor roaming. *arXiv preprint arXiv:2402.00763*, 2024. 3, 5
- [9] Michael Broxton, John Flynn, Ryan Overbeck, Daniel Erickson, Peter Hedman, Matthew Duvall, Jason Dourgarian, Jay Busch, Matt Whalen, and Paul Debevec. Immersive light field video with a layered mesh representation. *ACM TOG*, 39(4):86–1, 2020. 1
- [10] Angel Chang, Angela Dai, Thomas Funkhouser, Maciej Halber, Matthias Niebner, Manolis Savva, Shuran Song, Andy Zeng, and Yinda Zhang. Matterport3d: Learning from rgb-d data in indoor environments. In *2017 International Conference on 3D Vision (3DV)*, pages 667–676. IEEE, 2017. 1, 5, 2
- [11] David Charatan, Sizhe Lester Li, Andrea Tagliasacchi, and Vincent Sitzmann. pixelsplat: 3d gaussian splats from image pairs for scalable generalizable 3d reconstruction. In *CVPR*, pages 19457–19467, 2024. 2, 3
- [12] Anpei Chen, Zexiang Xu, Fuqiang Zhao, Xiaoshuai Zhang, Fanbo Xiang, Jingyi Yu, and Hao Su. Mvsnerf: Fast generalizable radiance field reconstruction from multi-view stereo. In *ICCV*, pages 14124–14133, 2021. 2
- [13] Rongsen Chen, Fang-Lue Zhang, Simon Finnie, Andrew Chalmers, and Taehyun Rhee. Casual 6-dof: free-viewpoint panorama using a handheld 360 camera. *IEEE TVCG*, 29(9): 3976–3988, 2022. 3
- [14] Yuedong Chen, Haofei Xu, Qianyi Wu, Chuanxia Zheng, Tat-Jen Cham, and Jianfei Cai. Explicit correspondence matching for generalizable neural radiance fields. *arXiv preprint arXiv:2304.12294*, 2023. 2
- [15] Yuedong Chen, Haofei Xu, Chuanxia Zheng, Bohan Zhuang, Marc Pollefeys, Andreas Geiger, Tat-Jen Cham, and Jianfei Cai. Mvsplat: Efficient 3d gaussian splatting from sparse multi-view images. In *ECCV*, pages 370–386. Springer, 2024. 2, 3, 4, 5, 6, 1
- [16] Zheng Chen, Yan-Pei Cao, Yuan-Chen Guo, Chen Wang, Ying Shan, and Song-Hai Zhang. Panogrf: generalizable spherical radiance fields for wide-baseline panoramas. *NeurIPS*, 36:6961–6985, 2023. 2, 3, 4, 5, 6
- [17] Changwoon Choi, Sang Min Kim, and Young Min Kim. Balanced spherical grid for egocentric view synthesis. In *CVPR*, pages 16590–16599, 2023. 3
- [18] Dongyoung Choi, Hyeonjoong Jang, and Min H Kim. Omnilocalrf: Omnidirectional local radiance fields from dynamic videos. In *CVPR*, pages 6871–6880, 2024. 3
- [19] Mohammad Reza Karimi Dastjerdi, Yannick Hold-Geoffroy, Jonathan Eisenmann, Siavash Khodadadeh, and Jean-François Lalonde. Guided co-modulated gan for 360° field of view extrapolation. In *3DV*, pages 475–485. IEEE, 2022. 3
- [20] Kangle Deng, Andrew Liu, Jun-Yan Zhu, and Deva Ramanan. Depth-supervised nerf: Fewer views and faster training for free. In *CVPR*, pages 12882–12891, 2022. 2
- [21] Yuan Dong, Chuan Fang, Liefeng Bo, Zilong Dong, and Ping Tan. Panocontext-former: Panoramic total scene understanding with a transformer. In *CVPR*, pages 28087–28097, 2024. 3
- [22] Xiaodong Gu, Zhiwen Fan, Siyu Zhu, Zuozhuo Dai, Feitong Tan, and Ping Tan. Cascade cost volume for high-resolution multi-view stereo and stereo matching. In *CVPR*, pages 2495–2504, 2020. 4
- [23] Tewodros Habtegebrial, Christiano Gava, Marcel Rogge, Didier Stricker, and Varun Jampani. Soms: Spherical novel view synthesis with soft occlusion multi-sphere images. In *CVPR*, pages 15725–15734, 2022. 2, 3, 5
- [24] Lukas Höllein, Ang Cao, Andrew Owens, Justin Johnson, and Matthias Nießner. Text2room: Extracting textured 3d meshes from 2d text-to-image models. In *ICCV*, pages 7909–7920, 2023. 3
- [25] Alain Hore and Djemel Ziou. Image quality metrics: Psnr vs. ssim. In *PR*, pages 2366–2369. IEEE, 2010. 6
- [26] Huajian Huang, Yingshu Chen, Tianjian Zhang, and Sai-Kit Yeung. 360roam: Real-time indoor roaming using geometry-aware 360° radiance fields. *arXiv preprint arXiv:2208.02705*, 2022. 3
- [27] Huajian Huang, Changkun Liu, Yipeng Zhu, Hui Cheng, Tristan Braud, and Sai-Kit Yeung. 360loc: A dataset and benchmark for omnidirectional visual localization with cross-device queries. In *CVPR*, pages 22314–22324, 2024. 1, 6, 2
- [28] Sangeek Hyun and Jae-Pil Heo. Adversarial generation of hierarchical gaussians for 3d generative model. In *NeurIPS*, 2024. 4
- [29] Hyeonjoong Jang, Andreas Meuleman, Dahyun Kang, Donggun Kim, Christian Richardt, and Min H Kim. Egocentric scene reconstruction from an omnidirectional video. *ACM TOG*, 41(4):1–12, 2022. 3

- [30] Hualie Jiang, Zhe Sheng, Siyu Zhu, Zilong Dong, and Rui Huang. Unifuse: Unidirectional fusion for 360 panorama depth estimation. *IEEE Robotics and Automation Letters*, 6(2):1519–1526, 2021. 4, 2
- [31] Bernhard Kerbl, Georgios Kopanas, Thomas Leimkühler, and George Drettakis. 3d gaussian splatting for real-time radiance field rendering. *ACM TOG*, 42(4):139–1, 2023. 2, 1
- [32] Hakyong Kim, Andreas Meuleman, Hyeonjoong Jang, James Tompkin, and Min H Kim. Omnisdf: Scene reconstruction using omnidirectional signed distance functions and adaptive binotrees. In *CVPR*, pages 20227–20236, 2024. 3
- [33] Benjamin Lefaudeux, Francisco Massa, Diana Liskovich, Wenhan Xiong, Vittorio Caggiano, Sean Naren, Min Xu, Jieru Hu, Marta Tintore, Susan Zhang, Patrick Labatut, Daniel Haziza, Luca Wehrstedt, Jeremy Reizenstein, and Grigory Sizov. xformers: A modular and hackable transformer modelling library. <https://github.com/facebookresearch/xformers>, 2022. 1
- [34] David Li, Yinda Zhang, Christian Häne, Danhang Tang, Amitabh Varshney, and Ruofei Du. Omnisyn: Synthesizing 360 videos with wide-baseline panoramas. In *2022 IEEE Conference on Virtual Reality and 3D User Interfaces Abstracts and Workshops (VRW)*, pages 670–671. IEEE, 2022. 2, 3, 4, 6
- [35] Hao Li, Yuanyuan Gao, Chenming Wu, Dingwen Zhang, Yalun Dai, Chen Zhao, Haocheng Feng, Errui Ding, Jingdong Wang, and Junwei Han. Ggrt: Towards pose-free generalizable 3d gaussian splatting in real-time. In *ECCV*, pages 325–341. Springer, 2024. 2, 5
- [36] Jisheng Li, Yuze He, Jinghui Jiao, Yubin Hu, Yuxing Han, and Jiangtao Wen. Extending 6-dof vr experience via multi-sphere images interpolation. In *ACM MM*, pages 4632–4640, 2021. 2
- [37] Longwei Li, Huajian Huang, Sai-Kit Yeung, and Hui Cheng. Omnigs: Omnidirectional gaussian splatting for fast radiance field reconstruction using omnidirectional images. *arXiv preprint arXiv:2404.03202*, 2024. 3, 5
- [38] Tsung-Yi Lin, Piotr Dollár, Ross Girshick, Kaiming He, Bharath Hariharan, and Serge Belongie. Feature pyramid networks for object detection. In *CVPR*, pages 2117–2125, 2017. 4, 1
- [39] Yuan Liu, Sida Peng, Lingjie Liu, Qianqian Wang, Peng Wang, Christian Theobalt, Xiaowei Zhou, and Wenping Wang. Neural rays for occlusion-aware image-based rendering. In *CVPR*, pages 7824–7833, 2022. 2, 3, 6
- [40] Ze Liu, Yutong Lin, Yue Cao, Han Hu, Yixuan Wei, Zheng Zhang, Stephen Lin, and Baining Guo. Swin transformer: Hierarchical vision transformer using shifted windows. In *ICCV*, pages 10012–10022, 2021. 4, 1
- [41] Ben Mildenhall, Pratul P Srinivasan, Matthew Tancik, Jonathan T Barron, Ravi Ramamoorthi, and Ren Ng. Nerf: Representing scenes as neural radiance fields for view synthesis. In *ECCV*, pages 405–421. Springer, 2020. 2, 6
- [42] Michael Niemeyer, Jonathan T Barron, Ben Mildenhall, Mehdi SM Sajjadi, Andreas Geiger, and Noha Radwan. Regularizing neural radiance fields for view synthesis from sparse inputs. In *CVPR*, pages 5480–5490, 2022. 2
- [43] Changgyoon Oh, Wonjune Cho, Yujeong Chae, Daehee Park, Lin Wang, and Kuk-Jin Yoon. Bips: Bi-modal indoor panorama synthesis via residual depth-aided adversarial learning. In *ECCV*, pages 352–371. Springer, 2022. 3
- [44] Ryan S Overbeck, Daniel Erickson, Daniel Evangelakos, Matt Pharr, and Paul Debevec. A system for acquiring, processing, and rendering panoramic light field stills for virtual reality. *ACM TOG*, 37(6):1–15, 2018. 1
- [45] Martin Roberts. How to evenly distribute points on a sphere more effectively than the canonical Fibonacci Lattice. <https://extremelarning.com.au/how-to-evenly-distribute-points-on-a-sphere-more-effectively-than-the-canonical-fibonacci-lattice/>, 2020. 3
- [46] Olaf Ronneberger, Philipp Fischer, and Thomas Brox. U-net: Convolutional networks for biomedical image segmentation. In *Medical Image Computing and Computer-Assisted Intervention—MICCAI 2015: 18th International Conference, Munich, Germany, October 5–9, 2015, Proceedings, Part III 18*, pages 234–241. Springer, 2015. 4
- [47] Julian Straub, Thomas Whelan, Lingni Ma, Yufan Chen, Erik Wijmans, Simon Green, Jakob J Engel, Raul Mur-Artal, Carl Ren, Shobhit Verma, et al. The replica dataset: A digital replica of indoor spaces. *arXiv preprint arXiv:1906.05797*, 2019. 5, 2
- [48] Shinya Sumikura, Mikiya Shibuya, and Ken Sakurada. Openvslam: A versatile visual slam framework. In *ACM MM*, pages 2292–2295, 2019. 6, 2
- [49] Yule Sun, Ang Lu, and Lu Yu. Weighted-to-spherically-uniform quality evaluation for omnidirectional video. *IEEE signal processing letters*, 24(9):1408–1412, 2017. 6
- [50] Shitao Tang, Fuyang Zhang, Jiacheng Chen, Peng Wang, and Yasutaka Furukawa. Mvdifffusion: Enabling holistic multi-view image generation with correspondence-aware diffusion. In *NeurIPS*, 2023. 3
- [51] Shengji Tang, Weicai Ye, Peng Ye, Weihao Lin, Yang Zhou, Tao Chen, and Wanli Ouyang. Hisplat: Hierarchical 3d gaussian splatting for generalizable sparse-view reconstruction. *arXiv preprint arXiv:2410.06245*, 2024. 2, 3
- [52] Prune Truong, Marie-Julie Rakotosaona, Fabian Manhardt, and Federico Tombari. Sparf: Neural radiance fields from sparse and noisy poses. In *CVPR*, pages 4190–4200, 2023. 2
- [53] Guangcong Wang, Yinuo Yang, Chen Change Loy, and Ziwei Liu. Stylelight: Hdr panorama generation for lighting estimation and editing. In *ECCV*, pages 477–492. Springer, 2022. 3
- [54] Jionghao Wang, Ziyu Chen, Jun Ling, Rong Xie, and Li Song. 360-degree panorama generation from few unregistered nfov images. In *ACM MM*, pages 6811–6821. ACM, 2023. 3
- [55] Qianqian Wang, Zhicheng Wang, Kyle Genova, Pratul P Srinivasan, Howard Zhou, Jonathan T Barron, Ricardo Martin-Brualla, Noah Snavely, and Thomas Funkhouser. Ibrnet: Learning multi-view image-based rendering. In *CVPR*, pages 4690–4699, 2021. 2, 3, 5, 6

- [56] Christopher Wewer, Kevin Raj, Eddy Ilg, Bernt Schiele, and Jan Eric Lenssen. latentsplat: Autoencoding variational gaussians for fast generalizable 3d reconstruction. *arXiv preprint arXiv:2403.16292*, 2024. 2, 5
- [57] Rundi Wu, Ben Mildenhall, Philipp Henzler, Keunhong Park, Ruiqi Gao, Daniel Watson, Pratul P Srinivasan, Dor Verbin, Jonathan T Barron, Ben Poole, et al. Reconfusion: 3d reconstruction with diffusion priors. In *CVPR*, pages 21551–21561, 2024. 2
- [58] Tianhao Wu, Chuanxia Zheng, and Tat-Jen Cham. Ipo-ldm: Depth-aided 360-degree indoor rgb panorama outpainting via latent diffusion model. *arXiv preprint arXiv:2307.03177*, 2023. 3
- [59] Haofei Xu, Jing Zhang, Jianfei Cai, Hamid Rezaatofghi, Fisher Yu, Dacheng Tao, and Andreas Geiger. Unifying flow, stereo and depth estimation. 2023. 4, 2
- [60] Haofei Xu, Anpei Chen, Yuedong Chen, Christos Sakaridis, Yulun Zhang, Marc Pollefeys, Andreas Geiger, and Fisher Yu. Murf: Multi-baseline radiance fields. In *CVPR*, pages 20041–20050, 2024. 2
- [61] Haofei Xu, Songyou Peng, Fangjinhua Wang, Hermann Blum, Daniel Barath, Andreas Geiger, and Marc Pollefeys. Depthsplat: Connecting gaussian splatting and depth. *arXiv preprint arXiv:2410.13862*, 2024. 2, 3
- [62] Bangbang Yang, Yinda Zhang, Yijin Li, Zhaopeng Cui, Sean Fanello, Hujun Bao, and Guofeng Zhang. Neural rendering in a room: amodal 3d understanding and free-viewpoint rendering for the closed scene composed of pre-captured objects. *ACM TOG*, 41(4):1–10, 2022. 3
- [63] Jiayu Yang, Wei Mao, Jose M Alvarez, and Miaomiao Liu. Cost volume pyramid based depth inference for multi-view stereo. In *CVPR*, pages 4877–4886, 2020. 4
- [64] Botao Ye, Sifei Liu, Haofei Xu, Xueting Li, Marc Pollefeys, Ming-Hsuan Yang, and Songyou Peng. No pose, no problem: Surprisingly simple 3d gaussian splats from sparse unposed images. *arXiv preprint arXiv:2410.24207*, 2024. 2
- [65] Weicai Ye, Chenhao Ji, Zheng Chen, Junyao Gao, Xiaoshui Huang, Song-Hai Zhang, Wanli Ouyang, Tong He, Cairong Zhao, and Guofeng Zhang. Diffpano: Scalable and consistent text to panorama generation with spherical epipolar-aware diffusion. *arXiv preprint arXiv:2410.24203*, 2024. 3
- [66] Zehao Yu, Songyou Peng, Michael Niemeyer, Torsten Sattler, and Andreas Geiger. Monosdf: Exploring monocular geometric cues for neural implicit surface reconstruction. *NeurIPS*, 35:25018–25032, 2022. 2
- [67] Cheng Zhang, Zhaopeng Cui, Cai Chen, Shuaicheng Liu, Bing Zeng, Hujun Bao, and Yinda Zhang. Deeppanocontext: Panoramic 3d scene understanding with holistic scene context graph and relation-based optimization. In *ICCV*, pages 12632–12641, 2021. 3
- [68] Cheng Zhang, Qianyi Wu, Camilo Cruz Gambardella, Xiaoshui Huang, Dinh Phung, Wanli Ouyang, and Jianfei Cai. Taming stable diffusion for text to 360 panorama image generation. In *CVPR*, pages 6347–6357, 2024. 3
- [69] Kai Zhang, Nick Kolkin, Sai Bi, Fujun Luan, Zexiang Xu, Eli Shechtman, and Noah Snavely. Arf: Artistic radiance fields. In *ECCV*, pages 717–733. Springer, 2022. 5
- [70] Kai Zhang, Sai Bi, Hao Tan, Yuanbo Xiangli, Nanxuan Zhao, Kalyan Sunkavalli, and Zexiang Xu. Gs-irm: Large reconstruction model for 3d gaussian splatting. In *ECCV*, pages 1–19. Springer, 2025. 2, 3
- [71] Richard Zhang, Phillip Isola, Alexei A. Efros, Eli Shechtman, and Oliver Wang. The unreasonable effectiveness of deep features as a perceptual metric. In *CVPR*, pages 586–595, 2018. 5, 6

PanSplat: 4K Panorama Synthesis with Feed-Forward Gaussian Splatting

Supplementary Material

The supplementary material is organized as follows. In Sec. A, we provide additional details on the network architectures. In Sec. B, we provide additional details on the Gaussian parameter prediction and rendering. In Sec. C, we provide additional details on the experiment settings. In Sec. D, we provide quantitative comparisons on narrow baselines. In Sec. E, we provide more ablation studies. In Sec. F, we provide details on extending to real data. In Sec. G, we provide details on scaling up to 4K resolution. Finally, in Sec. H, we provide details on the demo video.

A. Network Architectures

In Sec. 3 of the main paper, we present our PanSplat architecture in two parts: the Hierarchical Spherical Cost Volume (Sec. 3.2) and the Gaussian Heads (Sec. 3.3). Here, we provide additional details on the network architectures.

Hierarchical Spherical Cost Volume. For feature pyramid extraction, we adopt a FPN architecture [38] enhanced with a Swin Transformer [40]. The Swin Transformer consists of 6 Transformer blocks, each with a self-attention layer and a cross-view attention layer. We use the xFormers [33] library for the transformer-based network for better efficiency. We apply Swin Transformer to the coarsest level of the feature map from the FPN encoder, then upsample the feature map to different levels with the FPN decoder. The result is a feature pyramid with 4 levels, with channel dimensions of 128, 96, 64, 32 from the coarsest to the finest level. For hierarchical spherical cost volume refinement, we adopt a 2DU-Net [15] with cross-view attention at the bottleneck layer for each level. We set depth candidates to 128, 64, 32 and channel dimensions of 2D U-Net to 128, 64, 32 for each level, respectively.

Gaussian Heads. We adopt a lightweight 3-layer CNN architecture for each Gaussian head, with a kernel size of 3×3 and a stride of 1, to extract feature map \tilde{F}_i^l for each view i at level l . We then sample a feature vector from the feature maps for each Gaussian, based on the pixel location defined on the Fibonacci lattice. Finally, a linear layer is applied to predict the Gaussian parameters $(\mu_i^l, \alpha_i^l, \Sigma_i^l, c_i^l)$. Specifically, to estimate Gaussian centers μ_i^l , we first estimate the correlation vectors c_i^l , then apply the same operations used for the cost volume to get a depth, which is then unprojected to 3D coordinates as mentioned in Sec. 3.1 of the main paper. The opacity α_i^l is predicted as a scalar value, followed by a sigmoid activation to normalize it to $[0, 1]$. The covariance Σ is composed of scaling vectors and quaternions, where the scaling is calculated as predicted normalized vectors $s_i^l \in [s_{\min}, s_{\max}]$ multiplied by the pixel size. This re-

stricts the Gaussian to a similar scale as the pixel, accounting for the change in pixel size across different levels. The color c_i^l is represented as spherical harmonic coefficients.

B. Gaussian Parameter Prediction and Rendering Details

In Sec. 3.3 of the main paper, we introduce Gaussian heads with local operations and a cubemap renderer. Based on these two components, we propose a two-step deferred backpropagation technique to enable training at 4K resolution. Here, we provide additional details on the deferred backpropagation technique, as shown in Fig. B.1, as well as the two components it relies on.

Tiled Operation for Gaussian Heads. We mentioned in Sec. 3.3 of the main paper that we exploit the local operations in the Gaussian heads to enable tiled operation for inference and deferred backpropagation. To be more specific, the inputs to the Gaussian heads on different levels are evenly split into $N \times N$ tiles, then fed into the Gaussian heads separately. However, this naive tiled operation impacts the boundary value of the output tiles, due to the zero padding of each convolutional layer, leading to discontinuity at the tile boundaries. Instead, we refine this design to output results identical to the non-tiled operation with a pre-padding operation. First the inputs are padded by 3 pixels, to accommodate the field of perception of the Gaussian heads. The padding involves copying the border pixels of left and right sides to the opposite side, which ensures loop continuity of the spherical geometry. The top and bottom sides are padded with zeros. Then, the tile regions are enlarged by 3 pixels to include the above padding, and introduce a 3-pixel overlap between adjacent tiles. The output tiles are finally cropped to the original size, stitched to a continuous, full resolution output.

Details of Cubemap Renderer. One key component of two-step deferred backpropagation is the cubemap renderer, which provides a differentiable rendering pipeline for the spherical 3D Gaussian pyramid. As shown in Fig. B.1, the cubemap renderer renders 6 faces (front, back, left, right, top, bottom) of the cubemap separately, then stitches them into an equirectangular panorama. This allows sequential face rendering for memory efficiency or batched face rendering for speedup. We build the cubemap renderer based on the CUDA 3DGS renderer [31] that implements with perspective camera projection. After rendering each face, we apply a bilinear grid sampling to stitch the faces into an equirectangular panorama. Specifically, the coordinates of pixels in the equirectangular panorama are first transformed

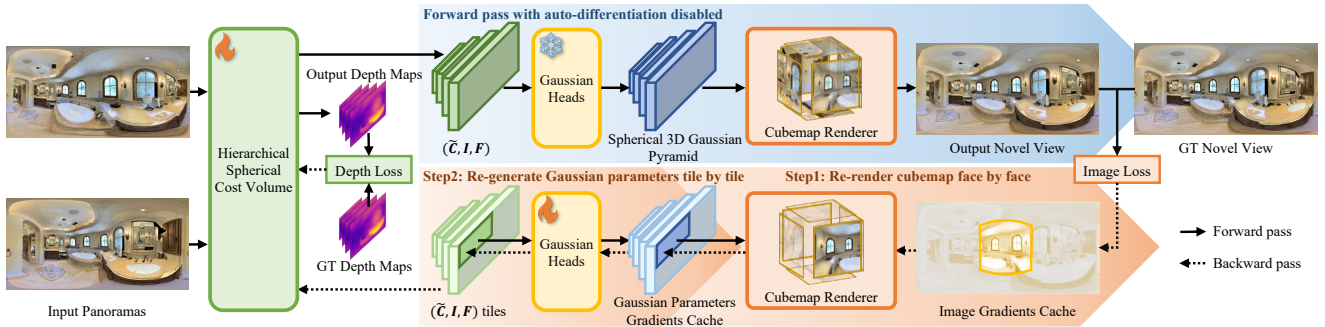


Figure B.1. **Two-step deferred backpropagation.** We propose a training strategy tailored for high-resolution panorama novel view synthesis. See Sec. B for details. *For simplicity, intermediate results of only a single view are shown.*

to the corresponding coordinates on the cubemap image. Then the pixel values are sampled from the cubemap image using bilinear interpolation. To achieve seamless stitching, we pad the edge pixels of the adjacent 4 faces to each face, ensuring the pixels interpolated on the edge have correct neighboring pixels from two nearby faces.

Details of Two-step Deferred Backpropagation. As shown in Fig. B.1, the two-step deferred backpropagation consists of a forward pass and two deferred backpropagation steps. Before the forward pass, we construct the hierarchical spherical cost volume with auto-differentiation on, and preserves the computational graph throughout the training step for efficiency. Then we disable auto-differentiation for a forward pass to render the full panorama. The full panorama is used for computing an image loss, with auto-differentiation on, to backpropagate and cache gradients to the image. Subsequently, we enable auto-differentiation and backpropagate gradients in two steps. In step one, the panorama is re-rendered face by face as cubemap to backpropagate and accumulate gradients to the Gaussian parameters. In step two, the Gaussian parameters are re-generated tile by tile, with gradients backpropagated and accumulated to the network parameters. Additionally, the gradients from the depth loss are accumulated to the network together with the gradients from the image loss. When training on real datasets without ground truth depth, the depth loss is replaced by auxiliary Gaussian heads and image loss as discussed in Sec. 3.4 of the main paper. In Sec. G, we provide more details on how the two-step deferred backpropagation saves memory consumption during training.

C. Experiment Details

High-resolution Synthetic Datasets. For synthetic data, we use the low-resolution (512×1024) synthetic datasets Matterport3D [10], Replica [47], and Residential [23] rendered by PanoGRF [16]. Additionally, we render two high-resolution datasets ($1024 \times 2048 / 2048 \times 4096$) using Matterport3D for fine-tuning. Specifically, we follow PanoGRF’s rendering protocol to render 6 perspective images at $512 \times 512 / 1024 \times 1024$ resolution respectively on

the cubemap faces, then stitch them into an equirectangular panorama image. We render 2 views with a baseline of 1.0 meter as input, and 1 view in the middle as the target view. The two datasets contain 5,000 / 2,000 samples for training. We render the test set in consistent with PanoGRF, with 10 samples for each dataset, which are used for demonstration in the demo video.

High-resolution Real Datasets. We use two real-world datasets to demonstrate generalization to real-world scenarios. For fine-tuning to real images, we use the 360Loc [27] dataset as it provides accurate pose registration from dense point cloud reconstructions and lidar scans. In addition, it is the largest dataset with high-resolution panoramic image sequences as far as we know, with 18 sequences (12 daytime and 6 nighttime) across 4 scenes, totaling 9,334 frames. We select one scene with 5 sequences as the test set, and fine-tune on the other 3 scenes with 13 sequences. When fine-tuning, we randomly sample two views spaced two frames apart as input, and use all four views as the target to calculate the loss. For analyzing image quality over different frame distances in Sec. F, we find that 360Loc is too sparse (average baseline of 0.47 meters) to provide a reasonable amount of frame distance samples. Therefore, we also capture a high-resolution Insta360 dataset with two sequences (one indoor and one outdoor) totaling 38K frames. Insta360 is recorded at 8K resolution and 24 FPS, later down-sampled to 4K for evaluation. We use OpenVSLAM [48] for camera pose estimation, disabling loop closure to avoid bad loop detection in repetitive environments. For evaluation purposes, we select two views spaced 15 frames apart as input, and evaluate all 17 frames. For evaluation on both datasets, we evenly sample 100 pairs of input views for each sequence, and average the results over all target views.

Implementation Details. We set the number of depth candidates D for the coarsest level to 128. Our model is implemented in PyTorch and trained on a single 80GB NVIDIA A100 GPU using the Adam optimizer with a learning rate of 2×10^{-4} . We use the pre-trained weights of UniMatch [59] to initialize the Swin Transformer of feature pyramid extractor. We also load the pre-trained weights of the monocular depth model [30] trained by PanoGRF [16] and freeze

Baseline Method	0.2m				0.5m			
	PSNR \uparrow	WS-PSNR \uparrow	SSIM \uparrow	LPIPS \downarrow	PSNR \uparrow	WS-PSNR \uparrow	SSIM \uparrow	LPIPS \downarrow
S-NeRF	20.79	19.52	0.697	0.376	17.95	16.81	0.628	0.486
OmniSyn	28.95	28.26	0.913	0.180	26.59	26.07	0.890	0.201
IBRNet	30.53	29.63	0.927	0.136	28.22	27.26	0.884	0.199
NeuRay	33.54	32.33	0.949	0.107	30.88	29.81	0.920	0.154
PanoGRF	34.29	33.27	0.952	0.098	31.41	30.46	0.924	0.132
MVSplat	32.93	32.98	0.955	0.063	31.55	31.62	0.943	0.075
PanSplat	33.92	34.00	0.959	0.066	32.46	32.53	0.950	0.072

Table D.1. **Quantitative comparison on narrow baselines.** We compare on Matterport3D under the baseline of 0.2 and 0.5 meters. Top results are highlighted in top1, top2, and top3.

it during training. Initially, we train the model on Matterport3D with an image height of 256 and a batch size of 6 for 10 epochs, then fine-tune it with an image height of 512 and a batch size of 2 for 5 epochs. For 4K Matterport3D fine-tuning, we gradually increase the resolution from a height of 1024 to 2048 over 3 epochs at each stage. To fine-tune on 4K 360Loc, we incrementally raise the resolution from a height of 512 to 1024 and finally 2048, with 65K, 26K, and 13K iterations for each stage, respectively. At resolutions of 1024 and 2048, we enable two-step deferred backpropagation with 4 and 16 tiles, setting batch sizes to 3 and 1, respectively. When fine-tuning on 360Loc at 1024 and 2048, we freeze the hierarchical spherical cost volume and only fine-tune the Gaussian heads. During evaluation, we generalize the model directly from Matterport3D to the Replica and Residential, and from 360Loc to the Insta360 dataset, without additional fine-tuning.

D. Quantitative Comparisons on Narrow Baselines

We follow the evaluation protocol of PanoGRF [16] to further evaluate on generalization to narrow baselines on Matterport3D. As shown in Tab. D.1, PanSplat achieves the best performance across most metrics, showing that our method generalizes well not only to wider baselines but also to narrow baselines.

E. More Ablation Studies

In Sec. 4.3 of the main paper, we conduct an ablation study to analyze the contributions of Fibonacci Gaussians and the 3D Gaussian pyramid. Here, we provide additional ablation studies in Tab. E.1 and Fig. E.1 to further analyze the impact of specific design choices in PanSplat.

Monocular Depth Features. We first ablate the use of monocular depth features in the hierarchical spherical cost volume (w/o Mono depth) in Tab. E.1. We note that integrating monocular depth features is a common practice in multi-view stereo methods [16, 61]. Although in our

Setup	WS-PSNR \uparrow	SSIM \uparrow	LPIPS \downarrow
w/o Mono depth	29.99	0.929	0.092
w/o 3DGP residual	29.35	0.922	0.102
w/o Hierarchical CV	28.04	0.857	0.180
w/o First three GHs	29.25	0.919	0.105
Full	30.01	0.931	0.091

Table E.1. **Full ablation study.** We evaluate the impact of certain design choices on PanSplat’s performance. Mono depth refers to integrating monocular depth feature from PanoGRF [16] to the hierarchical spherical cost volume, which is not our contribution and is insignificant to performance, but we include it in the Full model for the best results. Other design choices are ablated from the Full model, and significantly affect the performance.

case, the improvement is marginal, we include it in our final model for the best performance.

Residual Design of 3D Gaussian Pyramid. Second, we ablate the residual design of the Gaussian heads (w/o 3DGP residual), which leads to a significant drop in performance. To justify the performance gain from the residual design, we separately render the Gaussians from each level in Fig. E.1. It is shown that without the residual design, the coarsest two levels (Level #3 and #2) fail to output meaningful Gaussians, while the full model successfully distributes low frequency details to the coarser levels. This demonstrates the effectiveness of the residual design in guiding the Gaussian heads to capture multi-scale details.

Hierarchical Designs. Finally, we ablate the Hierarchical Cost Volume (w/o Hierarchical CV) and the First three Gaussian heads (w/o First 3 GH) respectively to analyze the joint impact of the two hierarchical designs. Similar to Sec. 4.3 of the main paper, for w/o Hierarchical CV, we replace the hierarchical cost volume with a single 1/4-resolution cost volume with 128 depth candidates to maintain comparable computational cost and memory usage. The removal of each of the two components hurts the performance significantly, indicating that the two hierarchical

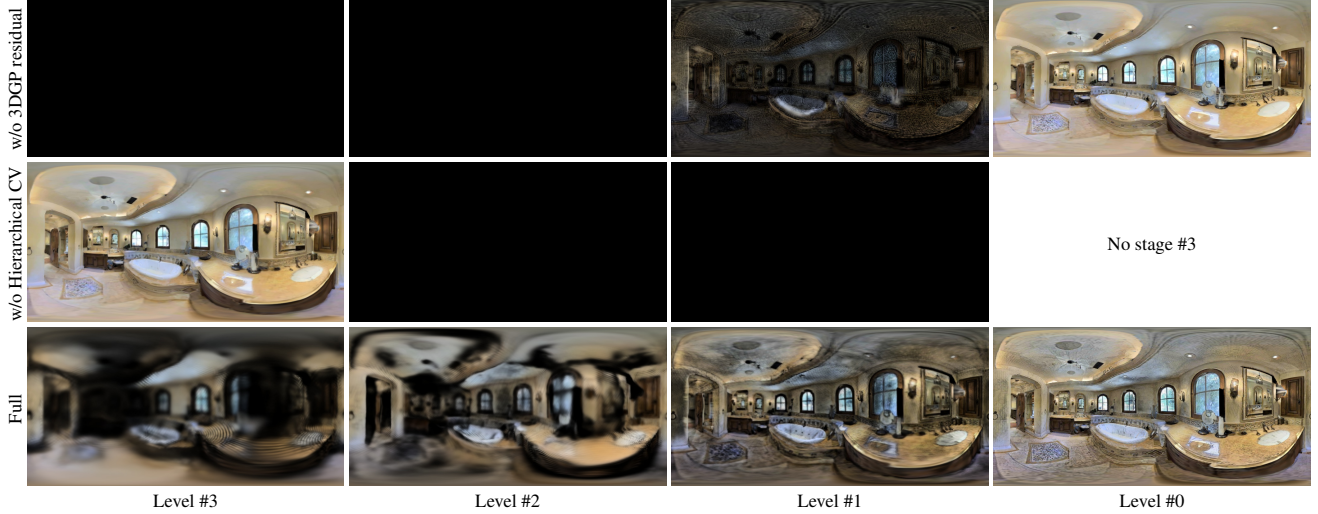


Figure E.1. **Visualization of 3D Gaussian Pyramid.** We visualize the rendering results of Gaussians from different levels of our 3D Gaussian Pyramid. Our full model (Full) successfully exploits the hierarchical structure of the 3D Gaussian Pyramid, where coarser levels mainly capture global structures and finer levels capture high-frequency details. In contrast, the ablated models (w/o 3DGP residual and w/o Hierarchical CV) fail to utilize all levels.

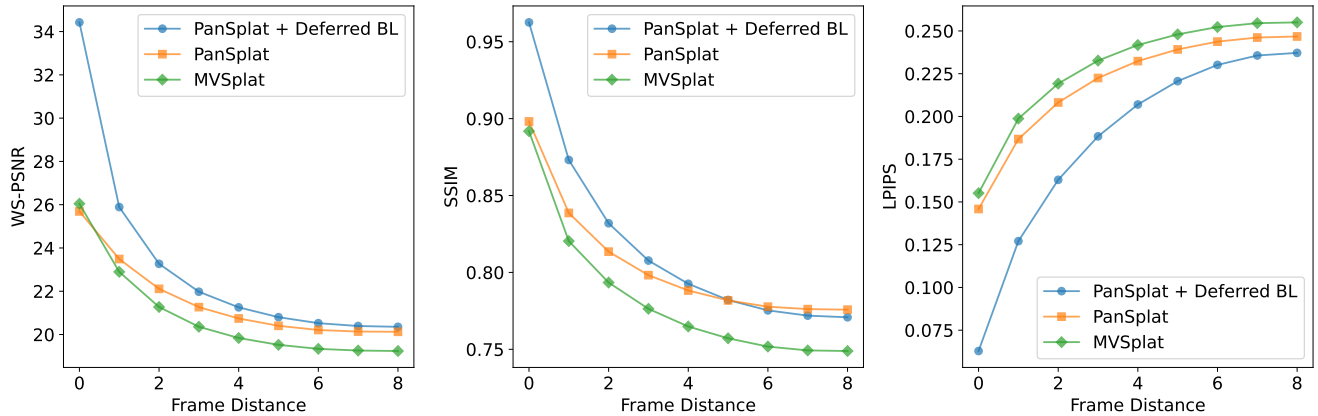


Figure F.1. **Quantitative comparisons on different frame distances.** We evaluate image quality metrics on Insta360 dataset with varying frame distances, comparing PanSplat with (PanSplat + Deferred BL) and without (PanSplat) deferred blending against MVSplat.

designs complement each other to achieve the best performance. We find that w/o Hierarchical CV tends to fall into local minima where only the coarsest level is utilized, as shown in Fig. E.1.

F. Extending to Real Data

Deferred Blending. In Sec. 3.3 of the main paper, we introduce a deferred blending technique to mitigate artifacts from misaligned Gaussians due to moving objects and depth inconsistencies. Here we provide additional details. Specifically, on real datasets, instead of directly consolidating the Gaussians from two input views for rendering, we first separately render them from the same target view into two different images, which we denote as $\{\tilde{I}_i\}_{i=0}^1$. Then we blend

them based on the distances d_i to the input views i by:

$$I = \frac{d_1 \tilde{I}_0 + d_0 \tilde{I}_1}{d_0 + d_1}. \quad (4)$$

The deferred blending aims to mitigate the influence of farther input view when rendering close to one of the input views, and relief the burden of matching moving objects.

Experiments. To evaluate the impact of deferred blending, we analyze the relationship between image quality (WS-PSNR, SSIM, and LPIPS) and frame distance (the number of frames between the target view and the nearest input view) on the Insta360 dataset. We compare PanSplat with (PanSplat + Deferred BL) and without (PanSplat) deferred blending, using MVSplat as a baseline. As shown in Fig. F.1, PanSplat consistently outperforms MVSplat

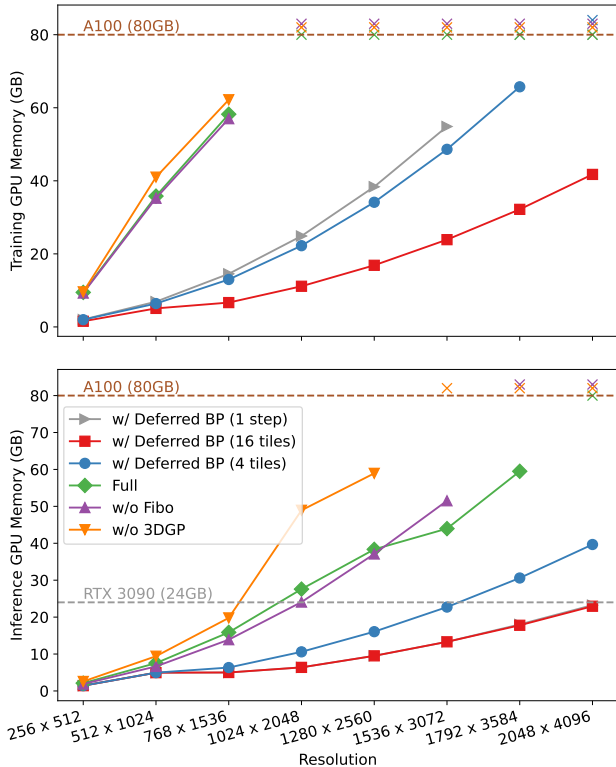


Figure G.1. **Full GPU memory consumption at different resolutions**, where \times indicates out-of-memory errors even on a 80GB A100. Note that w/ Deferred BP (1 step) is overlapped with w/ Deferred BP (16 tiles) for inference. Memory consumption is tested with a batch size of 1.

across all metrics and frame distances. In addition, deferred blending provides notable performance gains, especially when the frame distance is small. We further show visual comparisons on the 360Loc dataset in Figs. F.2 to F.5 and on the Insta360 dataset in Figs. F.6 to F.9. These results demonstrate that deferred blending significantly reduces artifacts arising from misaligned Gaussians (e.g., the dot pattern on the ceiling in Fig. F.7) and moving objects (e.g., the camera operator at the bottom in Fig. F.3). It also provides nearly perfect results when rendering at the same location as one of the input views by isolating the influence of the farther input view. This is particularly important for smooth transitions in virtual tours applications as shown in the demo video.

G. Scaling Up to 4K Resolution

In Sec. 4.3 of the main paper, we evaluate how two-step deferred backpropagation saves memory consumption during training. Here, we provide additional details on the both training and inference memory usage in Fig. G.1.

How do Fibo and 3DGP help save memory? Compar-

ing PanSplat (Full) with ablated versions (w/o Fibo, w/o 3DGP), we find that although the removal of 3D Gaussian pyramid (w/o 3DGP) introduces less Gaussians, it still consumes more memory due to slightly larger memory footprint of single cost volume. On the other hand, during inference, the removal of Fibonacci Gaussians (w/o Fibo) causes out-of-memory error starting from 1792×3584 resolution, a resolution that PanSplat can still support.

How does deferred backpropagation help save memory?

We then add deferred backpropagation (w/ Deferred BP) with tile settings of 2×2 (4 tiles) and 4×4 (16 tiles). As shown, the memory consumption drops significantly, with 16 tiles further enabling 4K inference on a 24GB RTX 3090 GPU. We use 4 tiles for fine-tuning at 1024×2048 resolution and 16 tiles for fine-tuning at 2048×4096 resolution, with a batch size of 3 and 1, respectively.

How does two-step design based on cubemap renderer help save memory?

We also include an ablated version with only step 2 of deferred backpropagation (1 step) with 16 tiles setting. The results show that the one-step version consumes significantly more memory than the two-step version when training, showing the effectiveness of cubemap renderer in reducing memory consumption. We note that the inference memory usage stays consistent as they share the same cubemap renderer with sequential face rendering.

H. Demo Video

By enabling 4K resolution support, PanSplat becomes a promising solution for immersive VR and virtual tours applications. We provide a demo video to demonstrate the superior image quality of PanSplat on diverse datasets, and to showcase its potential applications in real-world scenarios.

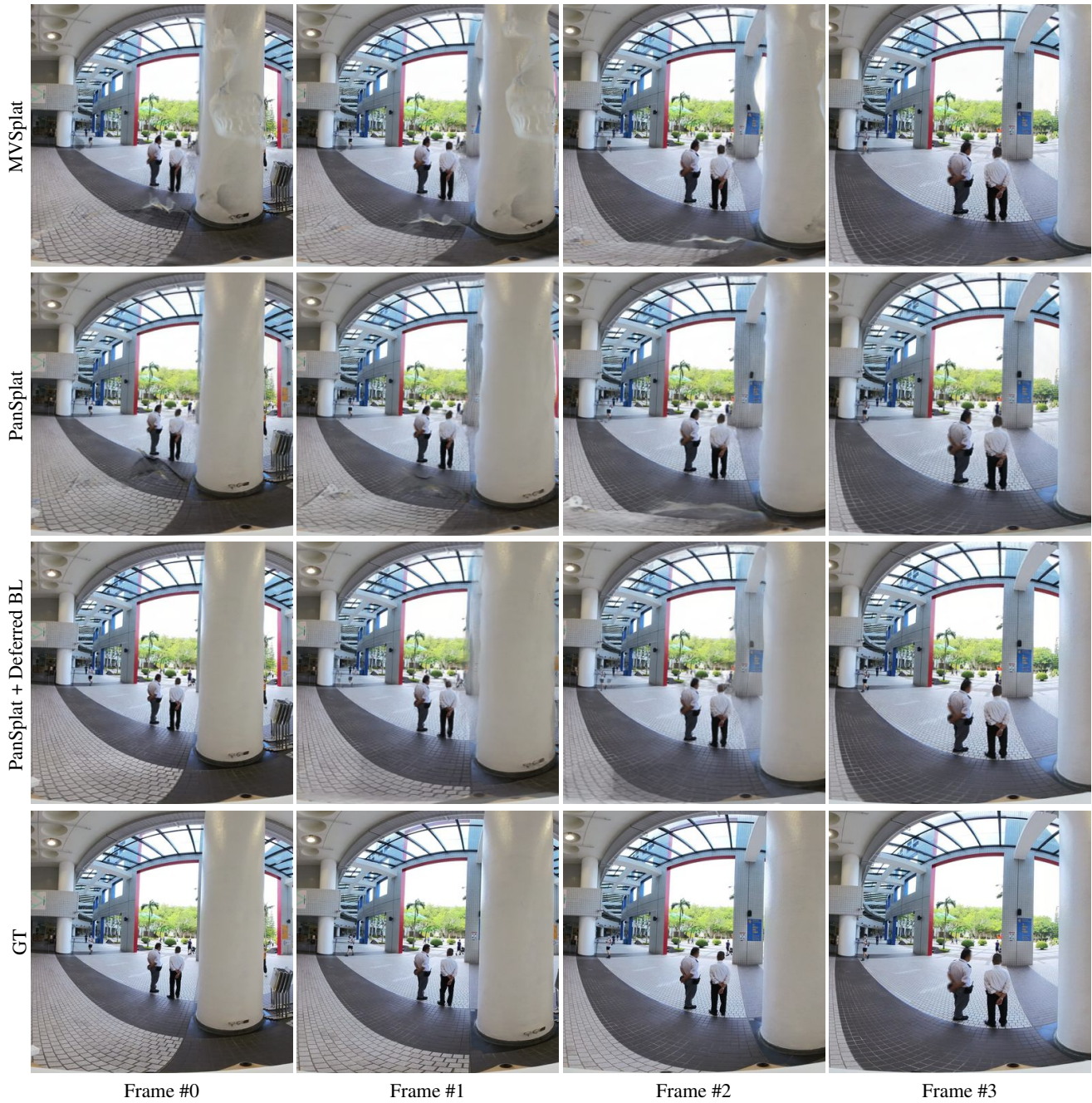


Figure F.2. **Qualitative comparisons on 360Loc dataset.** We show zoomed-in regions of the generated images by MV/Splat and PanSplat, with (PanSplat + Deferred BL) and without (PanSplat) deferred blending, compared to the ground truth (GT). The different columns represent different frames in the sequence, where Frame #0 and Frame #3 of GT are input views. We render the images across all four views to visualize different frame distances.



Figure F.3. **Qualitative comparisons on 360Loc dataset.** We show zoomed-in regions of the generated images by MV/Splat and PanSplat, with (PanSplat + Deferred BL) and without (PanSplat) deferred blending, compared to the ground truth (GT). The different columns represent different frames in the sequence, where Frame #0 and Frame #3 of GT are input views. We render the images across all four views to visualize different frame distances.

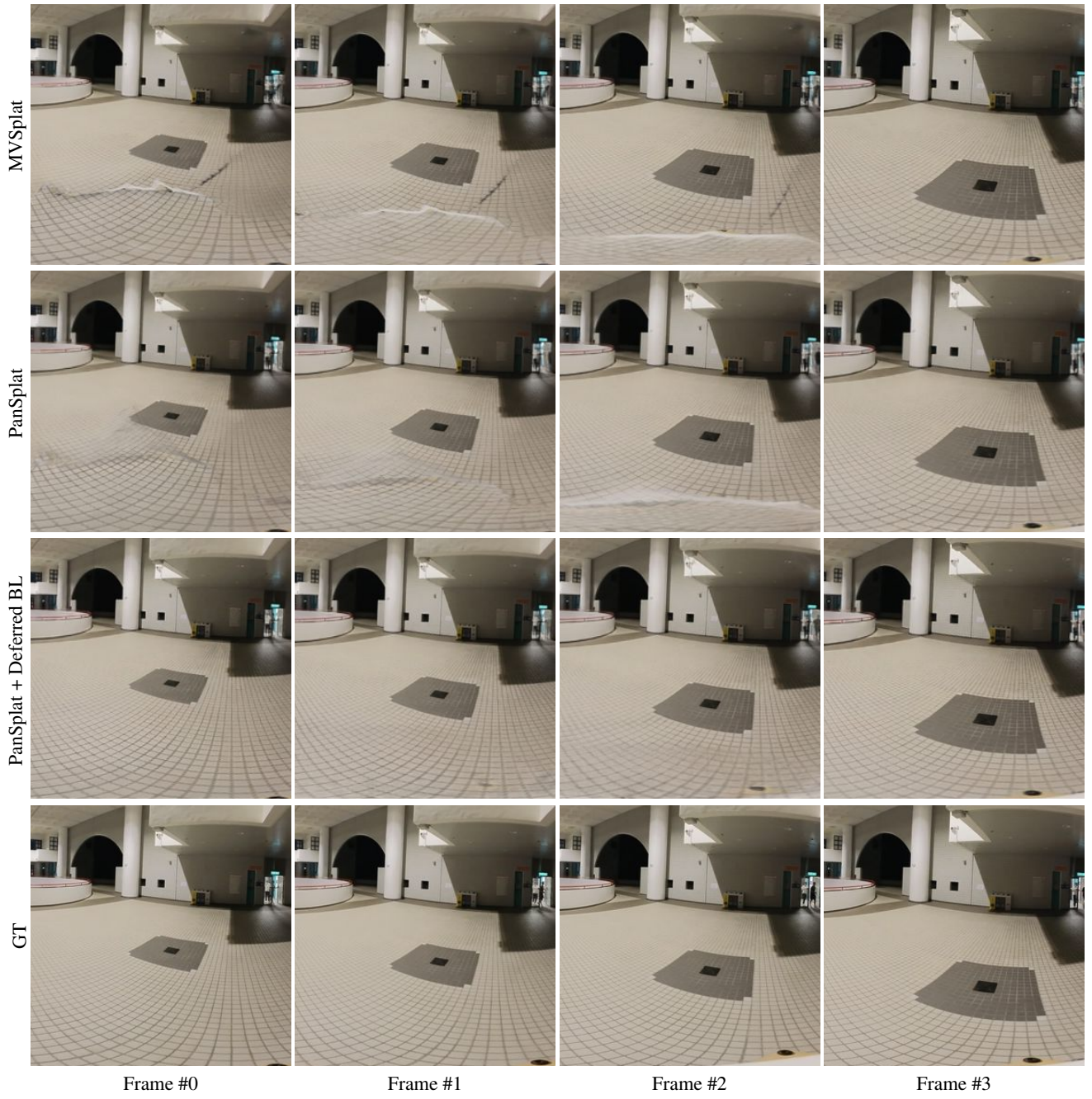


Figure F.4. **Qualitative comparisons on 360Loc dataset.** We show zoomed-in regions of the generated images by MV/Splat and PanSplat, with (PanSplat + Deferred BL) and without (PanSplat) deferred blending, compared to the ground truth (GT). The different columns represent different frames in the sequence, where Frame #0 and Frame #3 of GT are input views. We render the images across all four views to visualize different frame distances.

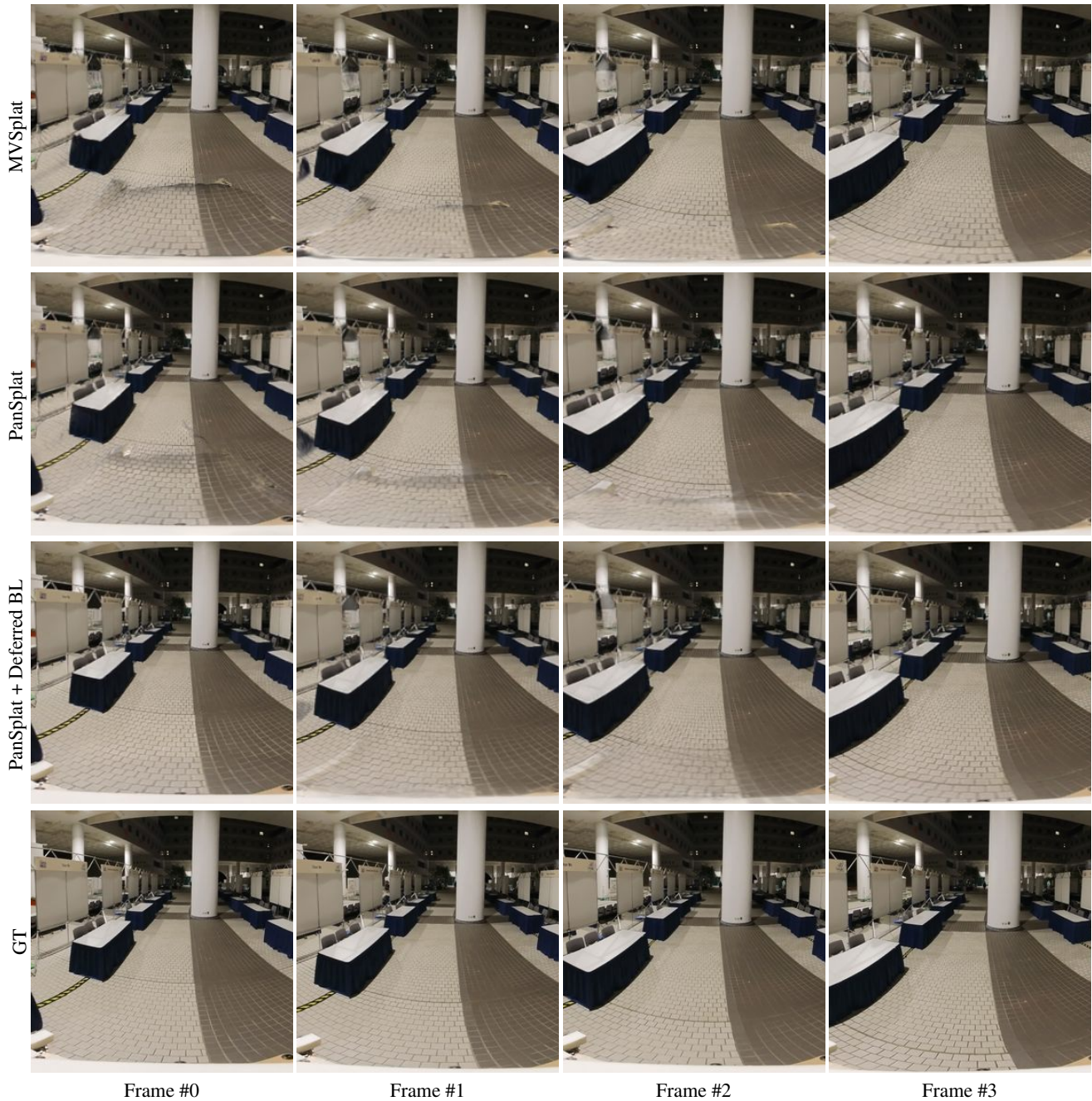


Figure F.5. **Qualitative comparisons on 360Loc dataset.** We show zoomed-in regions of the generated images by MV/Splat and PanSplat, with (PanSplat + Deferred BL) and without (PanSplat) deferred blending, compared to the ground truth (GT). The different columns represent different frames in the sequence, where Frame #0 and Frame #3 of GT are input views. We render the images across all four views to visualize different frame distances.

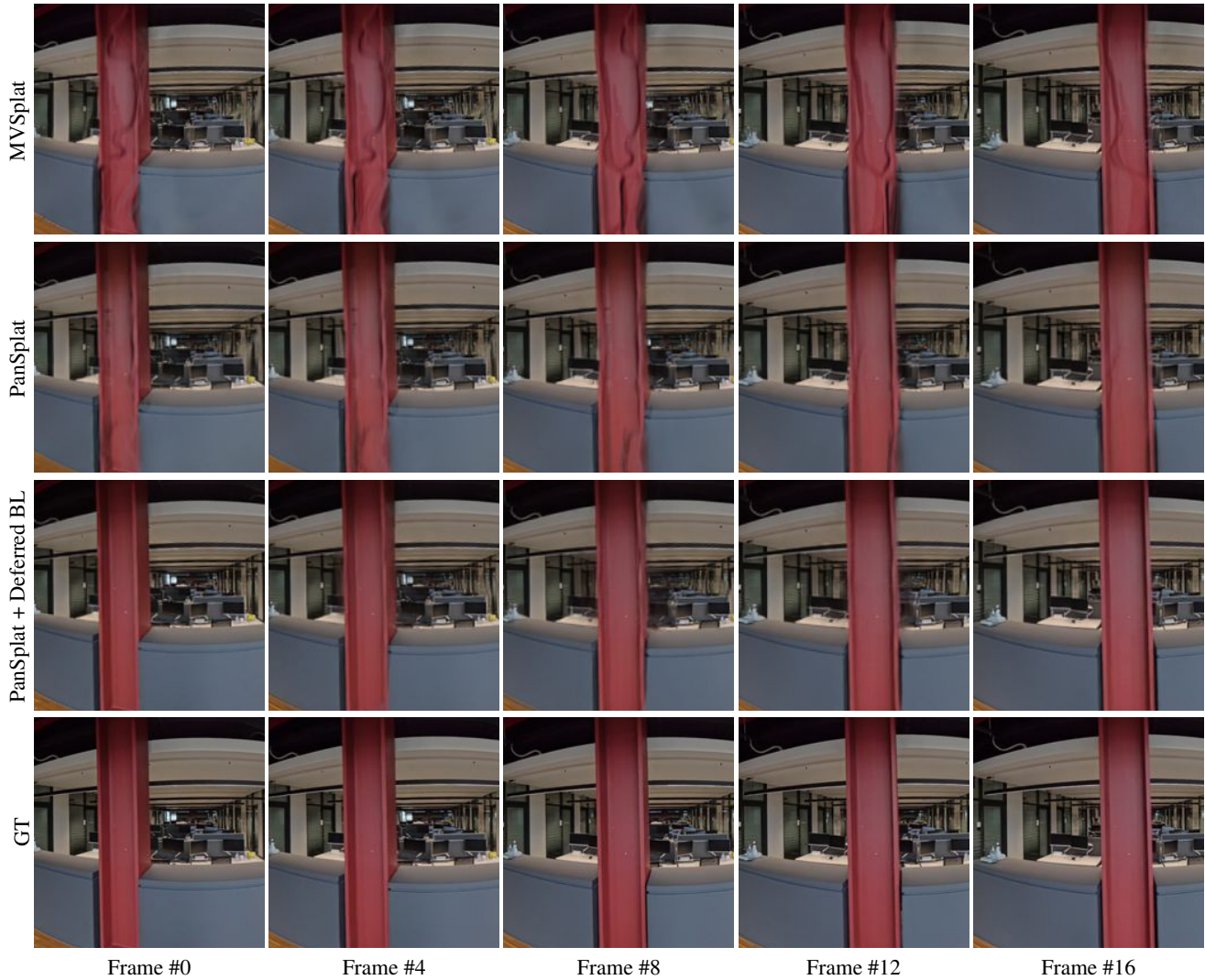


Figure F.6. **Qualitative comparisons on Insta360 dataset.** We show zoomed-in regions of the generated images by MV+Splat and Pan+Splat, with (Pan+Splat + Deferred BL) and without (Pan+Splat) deferred blending, compared to the ground truth (GT). The different columns represent different frames in the sequence, where Frame #0 and Frame #16 of GT are input views. We render the images across five evenly-spaced intermediate views to visualize different frame distances.

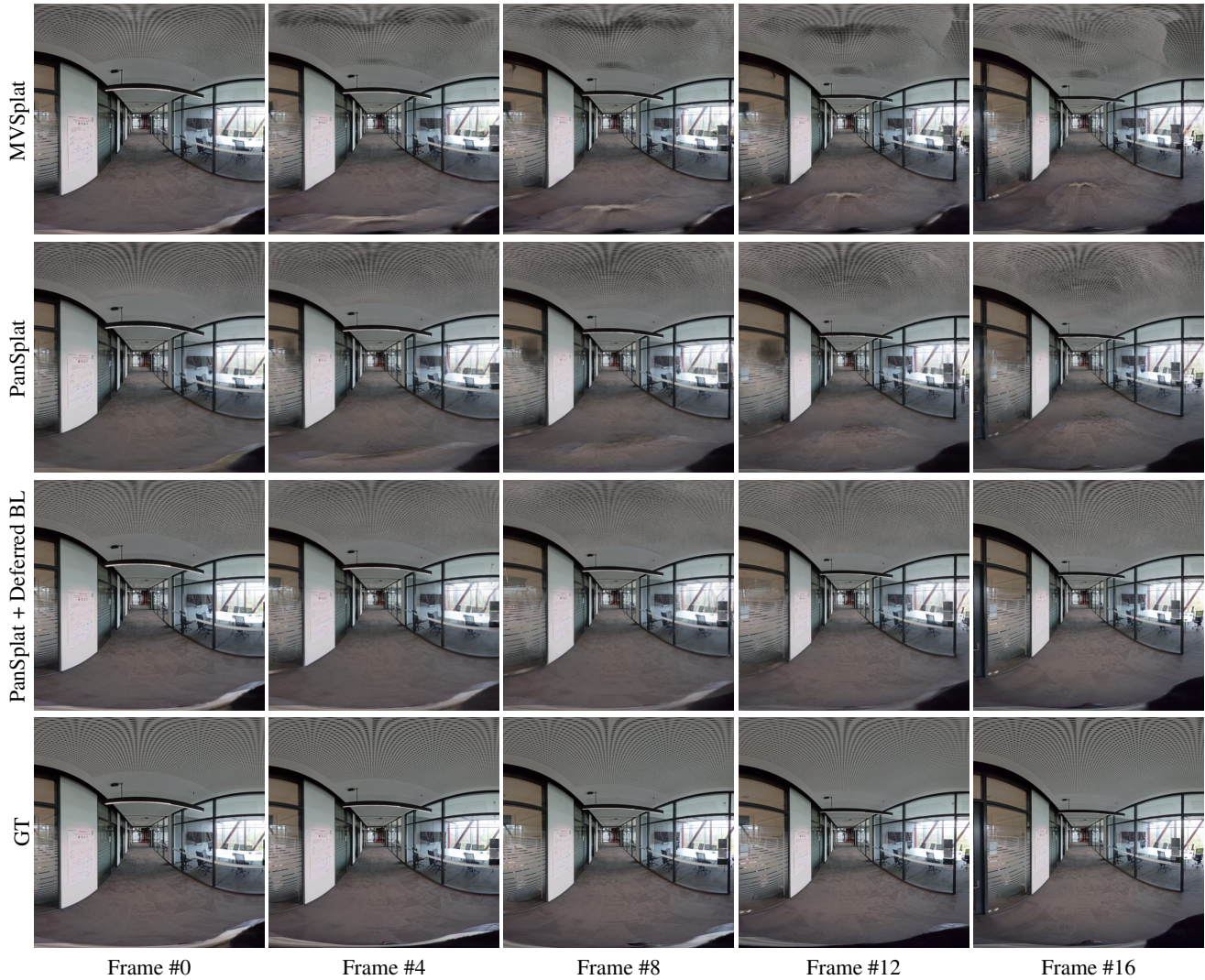


Figure F.7. **Qualitative comparisons on Insta360 dataset.** We show zoomed-in regions of the generated images by MV Splat and Pan Splat, with (Pan Splat + Deferred BL) and without (Pan Splat) deferred blending, compared to the ground truth (GT). The different columns represent different frames in the sequence, where Frame #0 and Frame #16 of GT are input views. We render the images across five evenly-spaced intermediate views to visualize different frame distances.

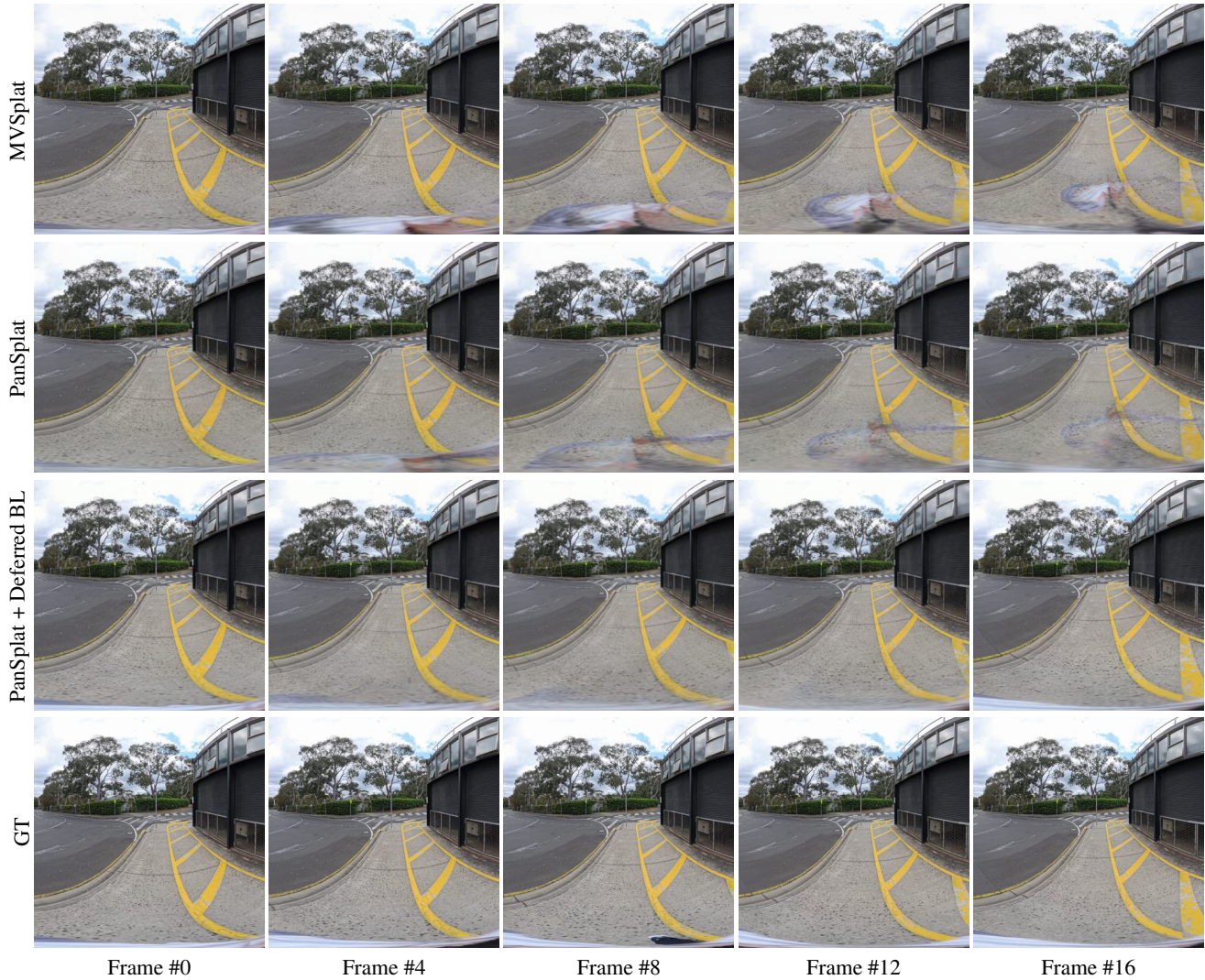


Figure F.8. **Qualitative comparisons on Insta360 dataset.** We show zoomed-in regions of the generated images by MV-Splat and Pan-Splat, with (Pan-Splat + Deferred BL) and without (Pan-Splat) deferred blending, compared to the ground truth (GT). The different columns represent different frames in the sequence, where Frame #0 and Frame #16 of GT are input views. We render the images across five evenly-spaced intermediate views to visualize different frame distances.

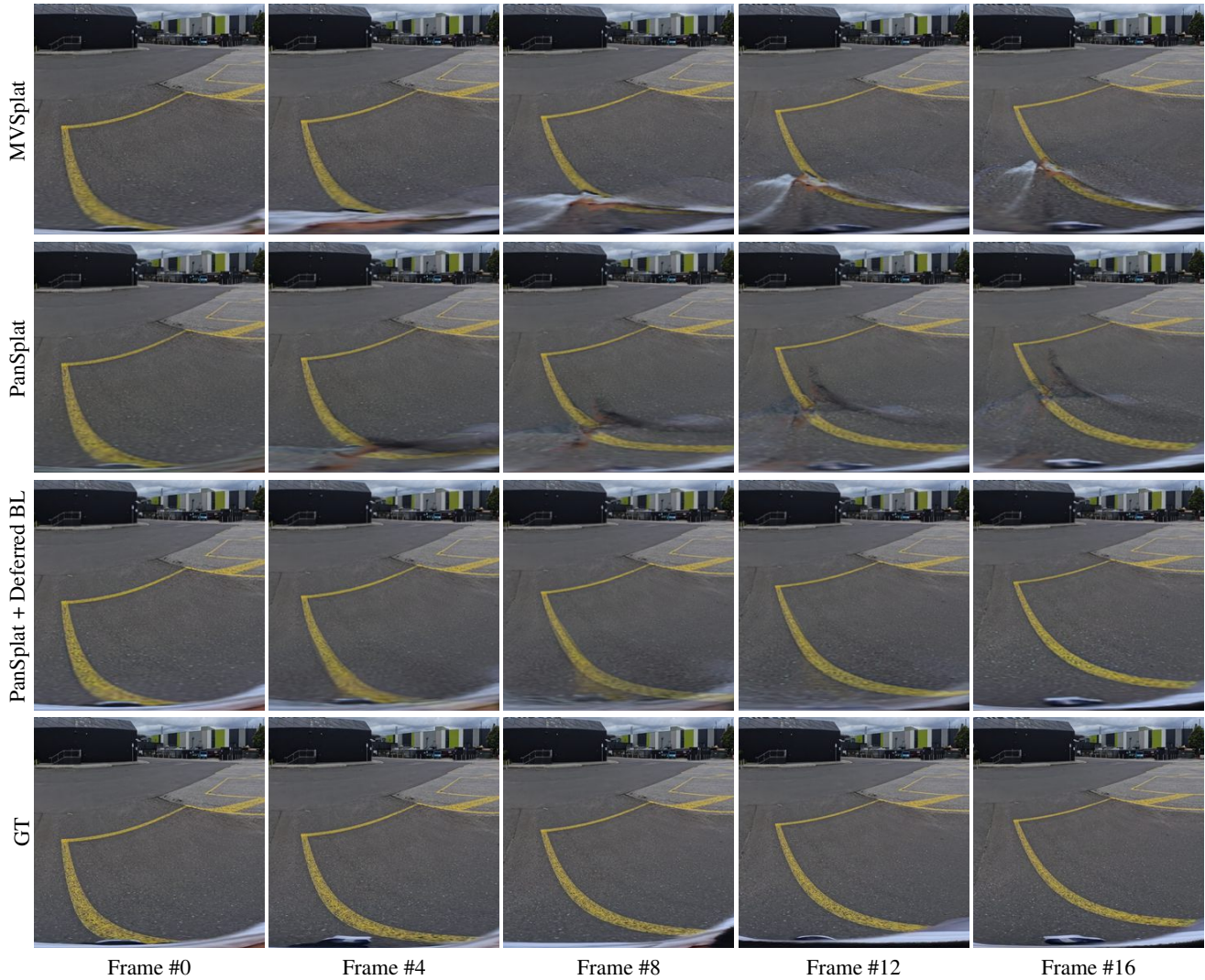


Figure F.9. **Qualitative comparisons on Insta360 dataset.** We show zoomed-in regions of the generated images by MV Splat and Pan Splat, with (Pan Splat + Deferred BL) and without (Pan Splat) deferred blending, compared to the ground truth (GT). The different columns represent different frames in the sequence, where Frame #0 and Frame #16 of GT are input views. We render the images across five evenly-spaced intermediate views to visualize different frame distances.